Electronic structures in overlayer systems

Anders Birk Sørensen

September 21th 2011

AALBORG UNIVERSITET

Institut for Fysik og Nanoteknologi
Skjernvej 4A
9220 Aalborg Øst
Telefon 99 40 92 15
Fax 99 40 92 35
http://www.nano.aau.dk

Electronic structures in overlayer systems

Master's thesis
Revised edition
September 2010 - September 2011
Advisor: Lars Diekhöner
Prints: 4
Number of pages: 62*
Finishing date: September 21th 2011

Anders Birk Sørensen

* Not including frontpage, title sheet, synopsis, foreword, contents and references.

Dansk resume

Dette speciale skulle oprindelige have handlet om temperaturprogrammeret desorption af CO fra pseudomorfisk kobolt på Cu(111). Desværre gav disse forsøg ikke nogen brugbare resultater, og forsøgene blev afbrudt. I stedet blev specialet drejet imod overfladetilstande og elektroniske strukturer i systemer tæt beslægtet med dem, som ellers skulle have været undersøgt.

Emnet i denne rapport er derfor endt med at være elektroniske strukturer i overlagssystemer. De systemer der refereres til er overlag af kobolt og sølv på en Cu(111)-krystal. Disse overlag har nogle karakteristiske træk ved pådampning på Cu(111). Koboltatomerne lægger sig i to atomlag tykke øer, som har overvejende trekantede udformninger. Det samler sig omkring de atomare trin på krystaloverfladen først, og begynder derefter at samle sig til øer på terrasserne. Sølv dampet på en Co/Cu(111)-prøve vil først lægge sig på toppen af koboltøerne, og sprede sig ud derfra i et enkelt atomlag. Først ved højere dækningsgrader begynder kobolt at danne højere øer, begyndende med et tredje lag på de eksisterende øer.

Ud over de oprindeligt planlagte TPD-forsøg, endte specialet med også at inkludere en række forsøg, som blev udført ved ASTRID i Århus. ASTRID er en lagerring, som benyttes til at generere intens stråling med høje fotonenergier. Den benyttede beamline leverede stråling i UV-området med fotonenergier fra 12 til 130eV. De målinger der beskrives her er fortrinsvist foretaget med fotonenergier på 23eV og 32eV.

Forsøgene drejede sig primært om overfladetilstandene, som er elektronbølger som er lokaliserede ved overfladen. Disse bølger har egenskaber som en næsten-fri elektrongas begrænset til overfladen. Ved at benytte vinkelopløst fotoelektronspektroskopi blev disse tilstande undersøgt eksperimentelt og forsøgt modificeret med variation af de pådampede mængder.

En række forsøg blev udført, og overfladetilstandene blev fittede med parabler hvor det var muligt. Ved at sammenligne parametrene for disse parabler, bindingsenergien i bunden E_0 og den effektive masse χ, viste der sig nogle regelmæssigheder.

For Ag/Cu(111)-preparationer var der et skift i energiniveauerne for Ag-tilstande, afhængigt af den pådampede mængde sølv. Ved tiltagende mængder sølv flyttede Ag-overfladetilstanden tættere på Ferminiveauet. Lignende resultater sås for Ag/Co/Cu(111)-preparationer, hvor sølvtilstandene blev forskudt

mod Ferminiveauet når mængden af underliggende kobolt blev forøget. Denne forskydning var dog ikke at se i kobber-tilstandene. Disse forholdte sig ved samme energier og effektive masser i alle præparationer, og blev ikke forskudt af tilstædeværelsen af hverken Ag eller Co overlag.

Under forsøgene kunne de eksakte dækningsgrader ikke bestemmes, og nogle af disse er derfor blevet bestemt senere, ved at sammenligne måledataene med forskellige referencer. De individuelle d-bånd er blevet fittet, og arealerne under dem er blevet brugt til at finde de sidste deponeringsrater og dækninggrader.

Oprindeligt var emnet begrænset til kemiske egenskaber af overflader, og disse er gennemgået teoretisk. Kemiske bindinger ved overflader er et resultat af overlappende orbitaler, og det kan derfor være nyttigt at kende de elektroniske egenskaber af de involverede komponenter. Den gennemgående teori for bindinger tager udgangspunkt i simple diatomige molekyler, hvor bindingen beskrives ved en enkelt elektron. Det vises at når atomernes orbitaler overlapper hinanden, finder der en opsplitning sted, som resulterer i to nye orbitaler.

Den samme mekanisme benyttes til at beskrive hvordan atomer bindes til en overflade. Når atomets orbitaler overlapper med valensbåndene i overfladen, vil der opstå en opsplitning som før. Den samme form for opsplitning finder sted i selve overfladen, hvor overlappende mellem atomerne breder orbitalerne ud til bånd indeholdende et kontinuum af tilstande (se figur 6.2 på side 45). Sådanne kontinuerte bånd kan ikke altid beregnes på helt samme måde som det var muligt for diatomige molekyler, og derfor introduceres Newns-Anderson-modellen.

Endeligt gennemgås de udførte TPD-forsøg. Forsøgsopstillingen gennemgås, og principperne bag TPD forklares. De opnåede data fremvises og forklares, og det diskuteres hvilke problemer der har været med opstillingen.

Foreword

This report is the written presentation of some of the experimental work I have carried out during the last two semesters of my physics programme at Aalborg University. I have written many longer reports before, but all of them have taken only a single semester, and most of them were written as group projects. Since this is the last work I will do before finishing my education, I chose to spend two semesters on it.

This was partly due to a wish to delve deeper into a subject than is possible during a single semester, and partly because previous experiences have shown, that experimentally oriented projects tend to be time consuming.

This report was It was originally intended that this project should be focussed on temperature programmed desorption of CO from various overlayer systems, but after some time and many experimental attempts it became obvious that these experiment would not bear fruit. Fortunately I was offered an opportunity to join my advisor, Associate Professor Lars Diekhöner, during a stay at the ASTRID storage ring at Århus University. While the experiments there were of a different nature, the new series of experiments did bring additional knowledge into the project regarding the electronic structures responsible for chemical bonding, the original primary topic of study.

Many thanks to my advisor, Associate Professor Lars Diekhöner, for his help and guidance in experimental technique, theoretical questions and for bringing me along during his stay at ASTRID.

Professor Emeritus Jens Onsgaard has provided additional guidance regarding the theory used to find coverages and deposition rates, as well as been one of the primary participants during the stay at ASTRID. I would also like to thank PhD student Mehdi Araz for his assistance in the laboratory.

Contents

Chapter 1

Introduction

This master's project was originally intended to be a study of chemical bonding at surfaces and modification of chemical properties by surface structures. The first 8 months of the year-long project were also spent building and testing an experimental setup for TPD, and this was used to conduct a series of desorption experiments using CO and cobalt deposited on different noble metals.

When one metal is deposited onto another, it will form different structures, depending on a number of factors. In the case of cobalt deposited onto copper, the growth is pseudomorphic, that is, the cobalt will conform to the structure and lattice constant of the substrate. This is not the case for cobalt deposited on silver (or silver on cobalt), instead the cobalt assumes a reconstruction following a moire[1] pattern.

The goal of the TPD experiments was to measure whether the moire pattern reconstruction of cobalt on silver had an effect on chemical bonding, and what such an effect would be. STM and STS studies of cobalt on Ag(111) surfaces have shown an increase in the localized density of states, following the moire pattern [GNKB09]. Since chemical bonding is caused by interactions between electrons, local modifications of electronic states could potentially lead to new adsorption states on the surface.

Unfortunately the experimental TPD setup did not live up to the expectations, and the subject of surface reactivity was put on hold in favor of angle-resolved photoelectron spectroscopy of electronic surface states. The TPD experiments had been directed at cobalt lying freely on the surfaces, however the system studied using ARPES was silver-capped cobalt islands on copper. Although the systems were different, they are still closely related both in substrate and the cobalt nanoislands. Therefore, despite the change of experimental technique and studied properties, the work has still been centered around cobalt on noble metals, in particular Co/Cu(111).

After the TPD experiments were put on hold, I was offered to join my

---

[1] Moiré is a type of fabric with a characteristic structure. The fabric is "larger" in some areas than others, causing a constant localized bulging.

advisor, Associate Professor Lars Diekhöner, during a one week stay at the Institute of Synchrotron Facilities in Aarhus. Here it was possible to perform ARPES at high resolutions due to the high intensity UV radiation coming from ASTRID, a storage ring used to provide synchrotron radiation for a range of experiments.

Surface states in silver overlayers on Cu(111) surfaces have previously been studied by other authors, and they have come to the conclusion that the onset of the states is dependent on the amount of silver deposited, and thereby (for coverages below one monolayer) the size of the silver islands [WWB$^+$04]. The surface states on bulk Ag(111) has also been studied [MBR02]. Morgenstern et al. has shown, using STS and *2-Photon PhotoEmission*, that the Ag surface states shift to lower binding energies with decreasing terrace size. This further supports the idea that the size of the surface structures are a key influence on the energy levels of the surface states.

Another possible modifier of surface electronic states is the periodic modulation of the moire pattern reconstruction. Pseudomorphic Co/Cu(111) islands capped with silver will not only have a moire pattern reconstruction on top, but also a modulated potential [BWDK09]. If the periodicity of the moire pattern is comparable to the wavelength of an electron in a surface state, Bragg reflection could potentially occur.

Before any treatment of electronic properties is begun, the overlayer structures will be described. The behavior of cobalt on noble metal surfaces is described using STM images and references to research literature. Silver on top of the cobalt structures is also described.

Following that, theoretical chapters on surface states and photoelectron spectroscopy follows to provide an intriduction to some of the properties measured and the method used. It's explained how surface states behave as nearly-free electrons on the surface of a metal, and it's suggested that surface steps could provide potential barriers to modify the properties of these surface states. Photoelectron spectroscopy is described using the three-step model, in which an electron is excited into a state with a higher energy, transported through the crystal, emitted into the vacuum and analysed.

The experimental results are then presented along with a description of the data treatment that has been performed, including how the surface cverage was found by comparing measured results to references, and by studying the d-band photoionisation cross-sections. A range of results are presented including energy distribution curves for the valence band states in the samples. The experimental measurements of the surface states are, of course, also presented and some general tendencies in their parameters are discovered. In short, it appears that the properties of surface states can be modified by putting small amounts of Co under layers of Ag. It's speculated that these shifts are a result of the surface states interacting with the steps as potential barriers.

After the electronic structures have been discussed, the report returns to the original topic, chemical bonding. In a theoretical chapter the basis for chemical bonds is discussed, starting with diatomic molecules. The theory is then built up to finally arive at bonding at surfaces, the original topic of study.

The inconclusive TPD experiments are presented at last along with a discussion of the problems that led to the change of subject, as well as possible improvements and fixes to the problems.

Chapter 2

Overlayer structures on Cu(111) surfaces

Cobalt displays interesting behaviours on different closely packed noble metal surfaces, most notably the formation of triangular and hexagonal islands. These islands have different sizes, shapes and heights depending on the amount of cobalt deposited, the choice of substrate and the substrate temperature during deposition. They do, however, have a general tendency to form islands multiple layers high with either a triangular or hexagonal shape.

Although only Ag/Co/Cu(111) were studied using ARPES (and to some extend Ag/Cu(111) and Co/Cu(111)), Co structures on other substrates were also studied using TPD. The total list of overlayer systems experimented an measured upon is:

- Co/Cu(111) - Reference for the TPD experiments
- Ag/Cu(111) - Used during ARPES experiments to approximate deposition rates
- Ag/Co/Cu(111) - The primary system studied using ARPES
- Co/Ag(111) - Primary interest in the TPD experiments
- Co/Au(111) - Also used for TPD

These systems, with the exception of Ag/Cu(111), are described here. STM images acquired in the STM laboratory at Aalborg University are also shown.

Co/Cu(111)

The cobalt islands on Cu(111) surfaces are triangular in shape, with sizes of $50-100$nm across at lower coverages. The cobalt nucleates around the atomic steps first, forming a dense band of structures very similar to the free-standing

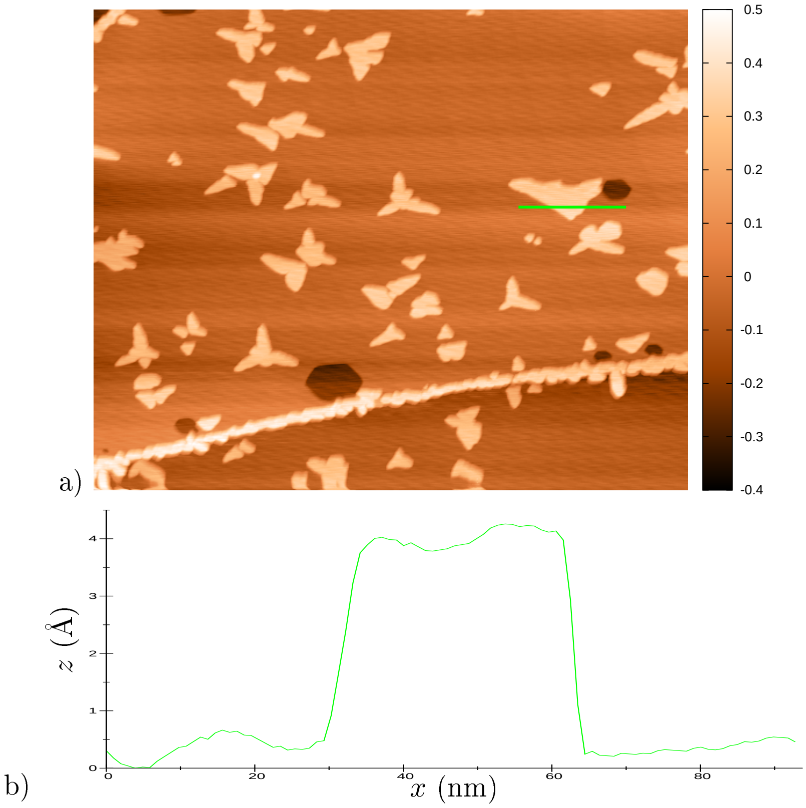

Figure 2.1: **a)** STM image of Co islands on a Cu(111) substrate. The Co initially nucleates around the surface steps and begins to form triangular islands at higher coverages. **b)** Height profile along the green line in the image. The Co islands are ~ 3.8Å tall with one additional layer below the substrate level.

islands. At lower coverages the islands are two layers tall, and a third layer doesn't begin to form until coverages of ~ 1.5ML (75% coverage by area). This holds for both the islands on the terraces and around the steps.

Cobalt in its bulk state has a lattice constant of 2.51Å in the close-packed plane (hcp structure). Copper has a lattice constant of 3.61Å in its fcc structure but the nearest-neighbor distance in the (111)-plane is only 2.55Å. The lattice mismatch of only 1.7% between the close-packed layers of cobalt and the Cu(111) surface results in pseudomorphic growth of Co nanoislands on the Cu(111) surface [LC98].

Ag/Co/Cu(111) sandwich layers

During the ARPES experiments, surface states in Ag/Co/Cu(111) systems have been studied. The basis for these samples are Co/Cu(111) samples with low CO coverages as described above, with the addition of a Ag overlayer.

The Ag overlayers initialy grow as only a single layer, and nucleates on top

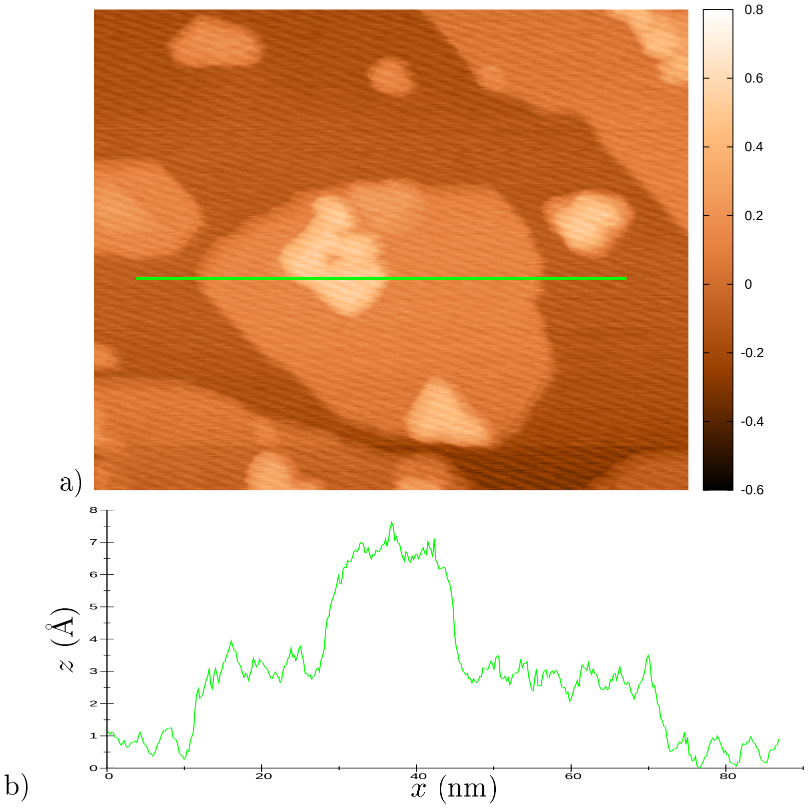

Figure 2.2: **a)** STM image of Ag-capped Co islands on a Cu(111) substrate. Ag deposited on Co/Cu(111) first nucleates on top of the Co and then spreads out around it. **b)** Height profile along the green line in the image.

of the Co islands. It grows out from there in larger islands still one layer thick. The deposited Ag islands have tall steps on them caused by the underlying Co. These steps the same height as the Co islands, nearly twice as tall as the steps on an Ag(111) surface. A layer of Ag is found both on the top of the islands and around it.

Ag does not grow pseudomorphically on Cu(111) and Co doe to a lattice mismatch of $\sim 13\%$. Instead the deposited Ag is rearranged into a moire pattern reconstruction on top of both the Co islands and the Cu(111) substrate.

Co/Ag(111)

The islands formed by deposited Co on Ag(111) are somewhat different from those on Cu(111). Just as Ag will not grow pseudomorphically on the Co islands, neither will Co grow pseudomorphically on Ag(111). Instead, islands of three to four layers in height are formed with the same moire pattern reconstruction as before. The moire pattern remains visible in islands of 7 layers

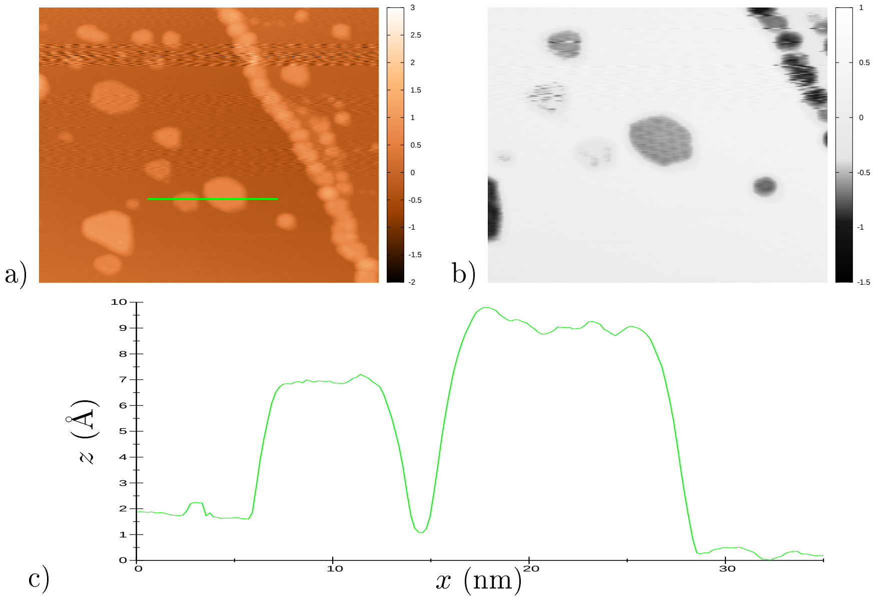

Figure 2.3: **a)** STM image of Co-islands on Ag(111). Co also nucleates on the steps on Ag(111), and forms islands on the terraces. the islands are not triangular but tend to be slightly hexgonal in shape. **b)** A crop of (a) with the color scale modified to show the moire pattern reconstruction. The island with the moire pattern visible is the larger of the two islands shown in the profile. **c)** Height profile along the green line in (a). The smaller island is 3 layers thick and the taller is 4.

thicknessref and can be seen in 4-layer islands using an STM, even at RT.

For preparations with the identical coverages (measured in ML), the islands on Ag(111) terraces have smaller surface areas than on Cu(111). This is a result of the taller islands. Figure 2.3a shows that the height of the islands is increased relative to Co/Cu(111), and therefore that an increased coverage (in ML) would be needed to obtain the same coverage by area as a Co/Cu(111) sample.

Find Co/Ag(111) reference

Co/Au(111)

Au(111) has a reconstruction of the surface atoms in a herringbone patternAu(111) herringbone ref. When Co is deposited onto Au(111), small Co islands begin to form in the elbows of the reconstruction, creating a periodic array of Co islands.

Find Co/Au(111) reference

The islands are two layers in height like Co/Cu(111), but are still smaller in surface area at identical coverages due to the increased number of islands.

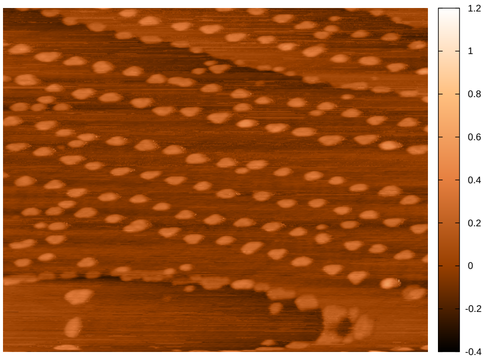

Figure 2.4: STM image of Co islands on Au(111). The islands have the same height as in figure 2.1. The islands are much smaller because the Co is divided into more islands. Au(111) has a zig-zag herringbone reconstruction (not visible in this image), and each Co island is placed in one of the reconstruction elbow-sites.

Chapter 3

Surface states

In this chapter, a short introduction to surface states will be given. The full derivations of the various properties will not be shown, but can be found in many textbooks.

Surface states are a form of electron waves that move only parallel to the surface, giving them the properties of a two-dimensional nearly-free electron gas. Since these waves are localised on the surface, they're also greatly dependent on surface features such as steps and deposited structures.

One of the surface properties studied here is the surface states of Ag/Co/Cu(111) structures. These structures are small islands of cobalt surrounded and covered by a single layer of silver. The large steps in the islands and the underlying layers of cobalt result in changes in the surface states, and the study of such systems could potentially lead to a better understanding of modification of surface states.

Ref til Shockley

3.1 Shockley state theory

Consider a one-dimensional crystal, ie. a string of atoms that stretch infinitely in both directions. The potential for such a crystal can be approximated in different ways, some more accurate than others. One model the the electrons wavefunctions is the nearly-free electron model. Here, the crystal potential is assumed to be weakly periodic, for example a cosine wave[Lüt01].

$$V(z) = \hat{V}\,\left[e^{i\frac{2\pi}{a}z} + e^{-i\frac{2\pi}{a}z}\right] = 2\hat{V}\,\cos\left(\frac{2\pi}{a}z\right)$$

This is actually a Fourier series, but since the atoms are assumed to be equally spaced, most of the terms vanish. A surface on this crystal can be modelled as a step in the potential.

With this approximation of the crystal potential in mind, solutions can be found for waves travelling inside the bulk material and near the surface.

The solutions for a wave travelling inside the bulk material can be found using *Bloch's theorem*[Kit05], and are often called *Bloch functions*.

Wavefunctions near the surface

Consider now an electron wave with wavenumber $k_\perp = \pm\frac{\pi}{a}$ travelling perpendicularly to the surface [1] in the one-dimensional crystal. This wave will be reflected by the step potential at the surface and give rise to another wave with wavenumber $k'_\perp = \mp\frac{\pi}{a} = k_\perp \mp \frac{2\pi}{a}$. By forming a linear combination of these two waves, the surface states can be expressed as

$$\psi_{\text{surf}} = A\, e^{i\, k_\perp \cdot z} + B\, e^{i\,\left(k_\perp - \frac{2\pi}{a}\right)\cdot z}\ .$$

To find the coefficients A and B, one must solve the *central equation* [Kit05]. The derivation of the solutions is not included hereInclude that sucker?. Instead the solution for this system is taken as-is from [Lüt01]. The solution consists of two parts, one exponentially decaying wave inside the crystal and one exponentially decaying non-oscillating part outside. The resulting state is a standing Bloch wave.

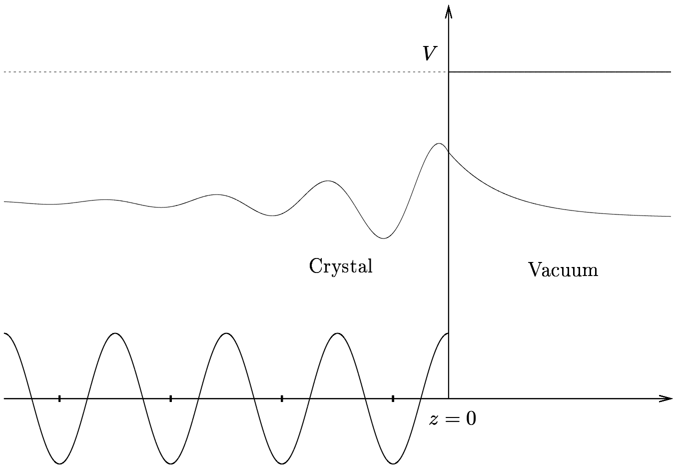

Figure 3.1: Sketch of a surface state in a periodic lattice. The crystal potential has been approximated by a periodic function, and the crystal edge is modelled at a step potential. A surface state is shown, exponentially decaying both into the crystal and out in the vacuum.

The waves shown above are only for a one-dimensional string of atoms. In most scenarios the studied systems will be three-dimensional and have a two-dimensional surface. This surface could be considered as the end of an

---

[1] We are interested in solutions near the Brillouin zone border, where $k = \pm\frac{G}{2} = \pm\frac{\pi}{a}$.

array of one-dimensional strings of atoms, ie. a 2D lattice with each unit cell being an instance of the model used above.

Since this surface is periodic, the potential affecting the surface states resembles a nearly-free electron system. The energy of an electron in such a system can be written as [2]

$$E_{\mathrm{S}}(k) = E_0 - \frac{\hbar^2 k^2}{2\,m^*} ,$$

where k is the magnitude of the wavevector of a wave travelling parallel to the surface, $m^* = \chi\, m_e$ is the effective electron mass (χ is the fractional mass) and E_0 is the energy of the state relative to the Fermi level at $k = 0$. Note that E_{S} is the energy relative to the Fermi level, and that is has a positive sign. The energy of this state starts at E_0 for $k = 0$, and then decreases in bond energy towards the Fermi level as the wavenumber is increased. So, in other words, the surface states considered here can be thought of as a nearly-free electron gas confined to the two-dimensional realm of the surface.

There are two main parameters that determine the behaviour of such a surface state: E_0 and χ (or m^*). The first parameter is the energy at the bottom of the state. This is indicative of how strongly the electrons in the surface states are bound to the substrate. The second is the effective mass, which tell us how "free" the electrons really are. If the effective mass is low, then so is the dispersion. It has been suggested that surface states can act as a charge carrier during surface reactions, and that low effective masses could speed up reaction rates by increasing interaction between adsorbed atoms and molecules.

Changes in energy and effective mass induced by surface structures

The electrons in surface states experience effects of the surface that electrons inside the bulk material would not. Such effects include surface steps and change of propagation medium due to deposited islands. Since the surface states are two-dimensional, they are greatly affected by structures on the surface, and each step represents a potential barrier.

There are many ways to affect these states. One is to reduce the size of the crystal terraces. This will reduce the intensity of surface states and eventually remove them entirely [MBR02]. The article cited here relates to Ag(111) surface states specifically, but the mechanism working here should also affect other surface states. More on harm. osc.

Since electrons in surface states are nearly-free, it is not unrealistic to consider them using a harmonic oscillator model. One approach would be to consider each terrace or deposited island as a quantum well, and use the

---

[2] This expression often appears with different signs. Here the energy of the state, E_{S}, is positive as well as E_0.

particle in a well of infinite depth model. In this model, it is assumed that the oscillating particle does not leave the well.

Reference to step-barrier article

Chapter 4

Photoelectron spectroscopy

The phenomenon behind photoelectron spectroscopy is the *photoelectric effect*, first characterised by Einstein. When high-energy electromagnetic radiation (UV or X-rays) hits a crystalline surface, electrons will become excited into a state from which they may leave the surface and enter the vacuum[1]. The energy of the electrons leaving the surface is

$$E_{\mathrm{kin}} = \hbar\omega - \phi - E_{\mathrm{B}} \ , \tag{4.1}$$

where E_{B} is the electron's binding energy, and ϕ is the work function[2], the amount of work required to move an electron to a point where is no longer interacts with the crystal.

By analysing the energy distribution and angle of these photoelectrons, one can measure various properties of the electronic structures inside the crystal.

PES experiments are divided into two types: UPS where UV light is used, and XPS where X-rays are used. The photon energies, $\hbar\omega$, in UPS experiments are typically in the $10 - 120\,\mathrm{eV}$ range, while XPS experiments use photon energies in the keV range.

4.1 Three-step model for photoemission

The most accurate model for photoemission is a one-step model, in which the entire process is treated as a single all-including transition. In the one-step model an electron is excited from an initial state into a so-called inverse LEED state[Hüf03]. In LEED experiments a sample is hit by a beam of electrons, which interacts with the sample, and results in a diffractive pattern being formed on a fluorescent screen. If this process was reversed, one would end up

---

[1] The photoelectric effect can be demonstrated by shining high intensity UV light onto a metal plate connected to a charged gold-leaf electroscope, discharging it by releasing the surplus electrons.

[2] ϕ is used as the work function here, but is used as an angle in the experimental section.

with an electronic state in the sample, which produces an outgoing beam of electrons. This is an inverse LEED state.

A more commonly used model for photoelectron spectroscopy is the *three-step model*, where, as the name implies, the photoemission process is simplified into three steps. The first step is the photoexcitation of the electrons, where the electrons are excited to a higher energy level. Then, the electrons may begin moving through the sample, under the assumption that momentum is conserved. Finally the electrons, given the right conditions, leave the sample and move into the vacuum. Although this is only a simplification, it still provides an insight into the processes behind the experimental technique employed and allows for discussion of the physical aspects of photoemission.

Excitation

The first step in the photoemission process is the optical excitation of an electron inside the crystal. With the crystal being perturbed by an electromagnetic field described by the vector potential $\mathbf{A} = \mathbf{A}(\mathbf{r}, t)$ and scalar potential $\varphi = \varphi(\mathbf{r}, t)$,[3] the probability of excitation from an initial to a final state, with wavefunctions ψ_i and ψ_f, respectively, is given by *Fermi's golden rule*[Lüt01]:

$$W_{f,i} = \frac{2\pi}{\hbar} m_{f,i} \, \delta \left(E_f(\mathbf{k}) - E_i(\mathbf{k}) - \hbar\omega \right) \ , \tag{4.2}$$

where

$$m_{f,i} = |< \psi_f, \mathbf{k} | H | \psi_i, \mathbf{k} >|^2 \ .$$

Dirac's δ-function is used to only include the pairs of initial and final states where the energy difference matches the photon energy.

The perturbation operator, H, is given by

$$H = \frac{e}{2m} \left(\mathbf{A} \cdot \mathbf{p} + \mathbf{p} \cdot \mathbf{A} \right) \ , \tag{4.3}$$

where $\mathbf{p} = i\hbar\nabla$ is the momentum operator. Equation (4.3) can be reduced, by assuming translational symmetry and using the Coulomb gauge ($\varphi = 0$) [Hüf03], to

$$H \approx \frac{e}{m} \mathbf{A} \cdot \mathbf{p} \ . \tag{4.4}$$

In UPS experiments the wavelength is usually between $\sim 10^3$Å and $\sim 10^2$Å. With wavelengths so large compared to the crystal periodicity, the vector potential is henceforth assumed a constant. Equation (4.2) is now entirely independent of time and location, and only considerations regarding energies remain.

---

[3] So that $\mathbf{E} = -\nabla\varphi - \frac{\partial \mathbf{A}}{\partial t}$ and $\mathbf{B} = \nabla \times \mathbf{A}$ [GPS02]. In the following the perturbation is assumed to be time-independent, and the partial derivative with respect to time is omitted.

The only electronic states that can be registered by this technique are those where the excited, final state is a wave moving towards the surface, ie. states having $k_\perp > 0$, and where the energy is large enough to overcome both the bond potential and the work function. For electrons satisfying these requirements, a flow of electrons arises inside the crystal. The intensity of electrons with energy E is given by

$$I^{\text{int}}(E, \hbar\omega, \mathbf{k}) \propto \sum_{f,i} W_{f,i} f(E_i) \delta(E - E_f(\mathbf{k}) \ . \tag{4.5}$$

This expression is a sum over all possible initial and final states. It's not strictly necessary to sum over both f and i since we have assumed direct excitations with no change in momentum, and each initial state only corresponds to one final state. If this were not the case, and an initial state could be excited into more than one final state, it would be difficult to distinguish between the crystal states when analysing the measurements. The same would apply if an initial state could be excited into multiple final states[4]. The Fermi function, $f(E_i)$, ensures that only transitions with an initial state energy, $E_i(\mathbf{k})$, below the Fermi level are included.

During this excitation process, many electrons will leave their initial states and, very briefly, leave these unoccupied. These states are occupied very quickly again by other electrons, diffusing the electron holes out into the entire crystal. The excitations only take place near the surface, leaving the electrons in the rest of the crystal to fill up the empty states.

Movement to the surface

After photoexcitation, the excited electrons must be transported to the surface before they can leave the crystal. Although the escape depth of photoelectrons is not particularly deep in UPS experiments, the emitted electrons can not be assumed to come exclusively from the top layer of atoms. There is always some degree of transmission from the lower layers, meaning that the emitted electrons will be a mix of electrons from both surface and initial bulk states.

The degree of mixing of bulk and surface states is mainly dependent on the *mean free electron path*, which is a measure for the average distance an electron can travel inside the crystal before being scattered by inelastic collisions. The electrons that have been scattered in this way lose part of their kinetic energy and have their momentum changed. The loss of kinetic energy makes it impossible to determine the binding energy of the electron in its initial state, and the change in momentum represents a lateral (and unpredictable) shift in the band structure.

---

[4] In reality indirect excitations do take place. In such cases the electrons can jump into several different final states, by converting some of the photon's energy to momentum.

Electron scattering can take place through a number of mechanisms, such as electron-electron collisions, and excitations of lattice and electron gas vibrations (phonon and plasmon collisions).

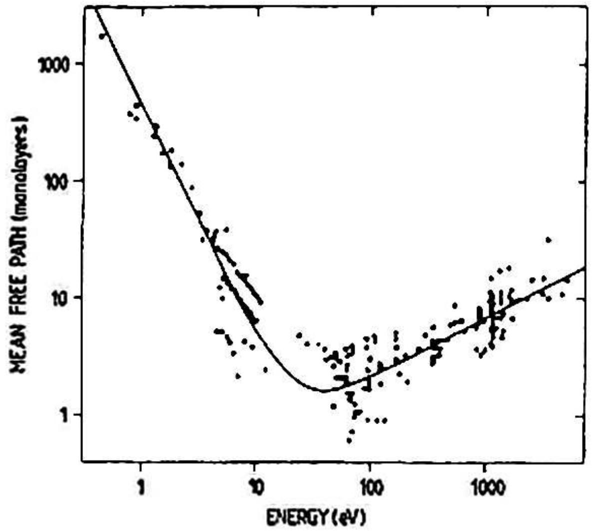

Figure 4.1: The mean free path of electrons in different solids plotted against electron energy. The mean free path is shortest for electron energies in the $10-100\,\mathrm{eV}$ range, indicating a short escape depth for electrons excited during UPS experiments. Taken from [Lüt01].

The probability of an electron being scattered on its way to the surface is inversely proportional to the mean free path. A long mean free path means that an electron can reach the surface from deep within the crystal without scattering, and a short mean free path means that electrons can only reach the surface from regions near the surface. Because of this, the *transport probability* is considered proportional to the mean free path.

$$D(E,\mathbf{k}) \propto \lambda(E,\mathbf{k}) \tag{4.6}$$

Although electrons deep inside the crystal may be excited by the incident light, the electrons far from the surface will not escape into the vacuum. As shown in figure 4.1, electrons with energies in the range discussed here will not escape from depths of more than a few layers. In the case of XPS with much higher photon energies, where the escape depth is much larger than in UPS experiments, the measured signal will have a much larger contribution from the states in the bulk.

Emission into vacuum

The final step in the three-step model is escape of the electron into the vacuum. After excitation and transport to the surface, the electrons must escape into the vacuum. In order for this to take place, the electrons must have enough momentum to overcome the work function and the potential barrier due to the crystal termination.

$$E_{\text{kin}} = \frac{\hbar^2 k_\perp^2}{2m} \geq E_{\text{vac}} - E_0$$

Here E_0 is the potential inside the crystal and E_{vac} is the potential in the vacuum. Electrons with insufficient energy to overcome the surface potential barrier will be reflected back into the crystal.

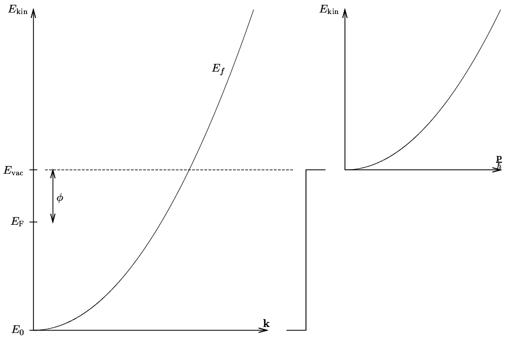

Figure 4.2: Energies of electrons in the excited final state inside and outside of the crystal. The electrons energy inside the crystal is $E_{\text{kin}} = \frac{\hbar^2 k^2}{2m^*}$ (left graph). The right graph shows the energy of the escaping electrons as a function of $\frac{\mathbf{p}}{\hbar}$, the momentum outside the crystal. Only electrons with an energy larger than $E_{\text{vac}} - E_0$ may escape.

The transversal component of the electrons momentum is conserved, so that

$$\mathbf{k}_{\parallel}^{\text{ex}} = \mathbf{k}_{\parallel} + \mathbf{G}_{\parallel} \tag{4.7}$$

The final step is described using the *escape cone* argument. The name refers to the cone of electron momenta that are sufficient to escape from the crystal. Figure 4.3 shows a sketch of this. The momentum of an escaping electron is conserved parallel to the surface, but not perpendicular to it. If the momentum is divided into two composants, one parallel to the surface and one perpendicular, only the perpendicular composant will be affected by the transition from sample to the vacuum. The parallel composant corresponds to oscillations along the surface, and these oscillations are not affected by the potential barrier when the electron passes the surface. The perpendicular composant represent oscillations across the potential barrier, and will be reduced by the transition.

As a result only electrons with momentum inside the cone (inside the crystal) escape to the surface[5]. The energy of the escaping electrons is

$$E_{\text{kin}} = \frac{\hbar^2 k^{\text{ex}\,2}}{2m} = \frac{\hbar^2}{2m}\left(k_{\parallel}^{\text{ex}\,2} + k_{\perp}^{\text{ex}\,2}\right) = E_f - E_{\text{vac}} \ , \tag{4.8}$$

where E_f is the energy of the excited final state, and E_{vac} is the vacuum energy level.

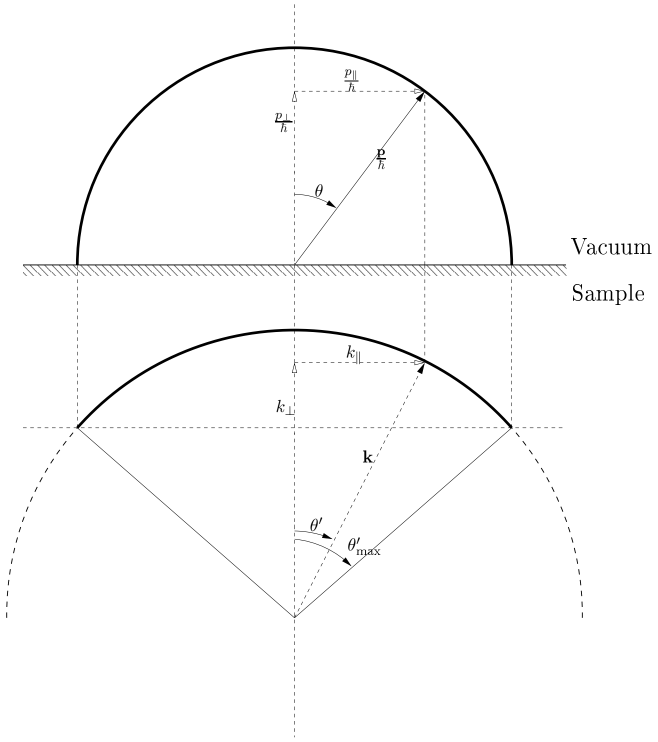

Figure 4.3: Sketch of the escape cones inside and outside of the crystal. The lower cone represents the states inside the sample, and the upper cone (hemisphere) represents the electrons that have escaped. The thick lines are lines of constant $|\mathbf{k}|$ and $\left|\frac{\mathbf{p}}{\hbar}\right|$. Although all electrons from states within the lower cone may escape, emitted electrons with small internal angles θ' can come from states with larger binding energies. Electrons with internal angles close to θ'_{max} can only escape if they come from states with low binding energies, limiting the range of detectable states to those near the Fermi level.

---

[5] This is very similar to the phenomenon of *Snell's window* from classical optics.

In addition to the requirement of a sufficient wave-vector component perpendicular to the surface, a transmission probability is also added. It is included though the *transmission rate*

$$T(E,\mathbf{k}) = \begin{cases} 0 & \text{for} \quad k_\perp^{\text{ex}2} < 0 \\ R \leq 1 & \text{for} \quad k_\perp^{\text{ex}2} > 0\ , \end{cases} , \tag{4.9}$$

with $k_\perp^{\text{ex}2} = \frac{2m}{\hbar^2} E_{\text{kin}} - k_\parallel^{\text{ex}2}$. R is the transmission probability.

Combining expressions (4.5), (4.6) and (4.9) yields an expression for the external, measurable electron intensity:

$$\begin{aligned} I^{\text{ex}}(E,\hbar\omega,\mathbf{k}_\parallel) =& I^{\text{int}}(E,\hbar\omega,\mathbf{k})\, D(E,\mathbf{k})\, T(E,\mathbf{k}) \delta\left(\mathbf{k}_\parallel + \mathbf{G}_\parallel - \mathbf{k}_\parallel\right) \\ & \propto \sum_{f,i} \frac{2\pi}{\hbar} m_{f,i}\, \delta\left(E_f(\mathbf{k}) - E_i(\mathbf{k}) - \hbar\omega\right) f(E_i) \delta(E - E_f(\mathbf{k}) \\ & \times \delta\left(\mathbf{k}_\parallel^{\text{ex}} - \mathbf{k}_\parallel + \mathbf{G}_\parallel\right) D(E,\mathbf{k})\, T(E,\mathbf{k}) \end{aligned}$$

Angle-resolved photoelectron spectroscopy

Studying emitted electrons at normal emission is an excellent tool to find the energy distributions, however angular resolution is needed if dispersions and values of $\mathbf{k}$ are to be found. Authors of many older papers using angle-resolved photoelectron spectroscopy have used a non-angle-resolved energy analyser, and achieved angle-resolution by recording multiple EDCs from different angles. Having an angle-resolved experimental setup, a setup that can analyse both the energy and direction of the emitted electrons, makes it much easier to study these dispersions, and allows for the measurements to be made in a shorter time. Since the sample is often cryogenically cooled during PES experiments, many trace gasses in the chamber will stick to the sample, pollution it and affecting the measurements.

Since the energy analyser disperses the electrons based on the angle from which they exit the sample, it is necessary to find a relation between the exit angles, θ and ϕ, and the wave-vector $\mathbf{k}_\parallel$.

Going from equation (4.8) this expression for the relationship between the emission angle and transversal wave number can be found:

$$\begin{aligned} k_\parallel^{\text{ex}} &= k^{\text{ex}} \sin\theta \\ &= \sqrt{\frac{2m}{\hbar^2} E_{\text{kin}}} \sin\theta \end{aligned} \tag{4.10}$$

Using this expression, it is possible to calculate the transversal wave-number, $k_\parallel = \left|\mathbf{k}_\parallel\right|$, of detected electrons, since $\mathbf{k}_\parallel$ is not changed when passing the surface.

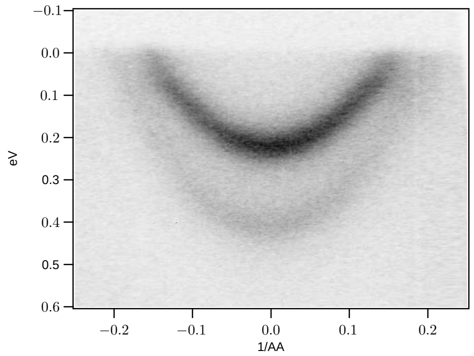

Figure 4.4: Example of an ARPES image showing the surface states of both Cu and Ag. The photon energy used was $h\nu = 23\text{eV}$. The surface state with the highest onset energy is the Ag state ($E_0 = 0.22\text{eV}$) and the lower is Cu ($E_0 = 0.39\text{eV}$).

4.2 Experimental setup

A photoelectron spectroscopy is composed of three main parts:

- A radiation source. This is usually either a gas discharge lamp, an X-ray tube or a synchrotron,
- The sample to be studied, and
- An energy analyser to measure the energy distribution of the emitted electrons.

Since electrons will not travel very far undisturbed through air or other gasses, it is also necessary to keep the setup under UHV conditions. This also keeps the sample clean. The experiments described here were conducted in the laboratory of prof. Philip Hofmann at Aarhus University, at the Institute of Storage Ring Facilities.

The radiation source used was *ASTRID* (Aarhus STorage Ring In Denmark), which is an electron storage ring used to produce synchrotron radiation. ASTRID has many beamlines able to provide radiation in many energy ranges. The particular beamline used here was the *SGM3* line. This line can deliver monochromatic UV radiation with photon energies from 12 eV to 130 eV at very high intensities, allowing for angle-resolved scans to be taken very quickly and with high resolution. Ref to SGM3 info page

The radiation from this beamline originates from an *undulator*, which is an array of magnets accelerating the electron beam up and down many times over a relatively short distance. With each “bend” on the electron path, a cone

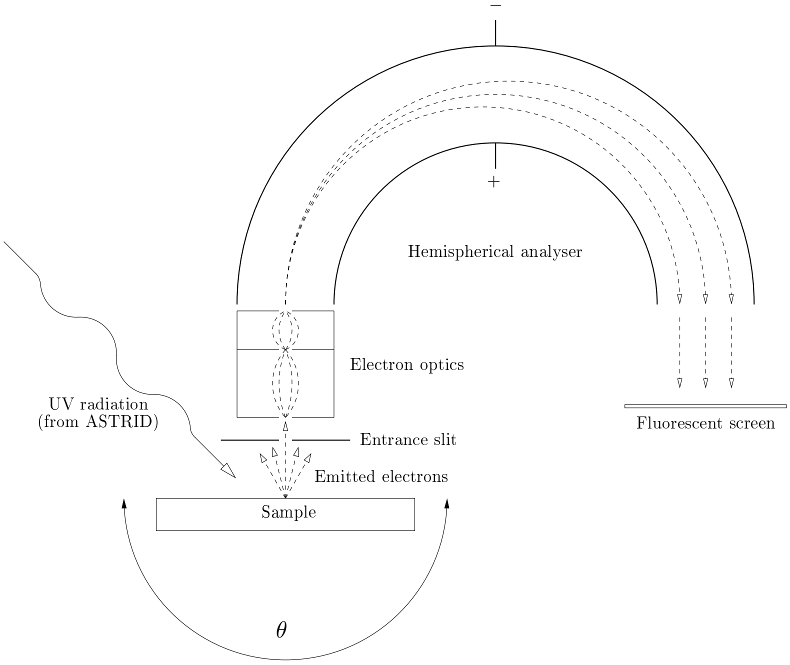

Figure 4.5: Experimental (AR)PES setup. Some of the ejected electrons pass through the opening in the entrance slit. They are passed through some electron optics for focusing. A retarding field may also be present. The 2D image formed on the fluorescent screen will be energy-resolved along one dimension, and angle-resolved along the other. The θ angle is changed by rotating the sample around an axis going out of the paper. The ϕ angle is around an axis lying in the paper, going from left to right.

of synchrotron radiation is emitted towards a computer controlled monochromator setup, allowing easy selection of photon energies.

At the end of the beamline is a UHV chamber with a main chamber for PES analysis and LEED measurements. There is also a separate preparation chamber for cleaning of the sample and deposition of metals. The base pressure of both chambers were in the mid 10^{-10} mbar range. Although this pressure is by no means bad or unusually high, it could have been lower. The UHV setup was a rather large and complicated construction, making baking only possible using heating cords and aluminium foil.

The main chamber has a helium-cooled sample manipulator, allowing for the sample to be kept at 67 K during ARPES measurements. Vertical movement of the manipulator was motorised, and rotation in one direction was computer controlled to allow for automated scans over 2D regions of the $\mathbf{k}_{\perp}^{\mathrm{ex}}$-space. Rotation along the other axisIs “the other axis” the proper term? could only be done by rotating a large knob inside the chamber using the wobblestick.

This was not intended for frequent adjustments.

The emitted electrons are analysed by a *Specs Phoibos 150 hemispherical energy analyser*. A hemispherical energy analyser consists of two concentric hemispheres with an electrostatic potential between them (figure 4.5). The electrons enter the analyser through an entrance slit, limiting the entering electrons to a plane cross section of the escape cone. The slit is oriented perpendicular to the analyser potential.

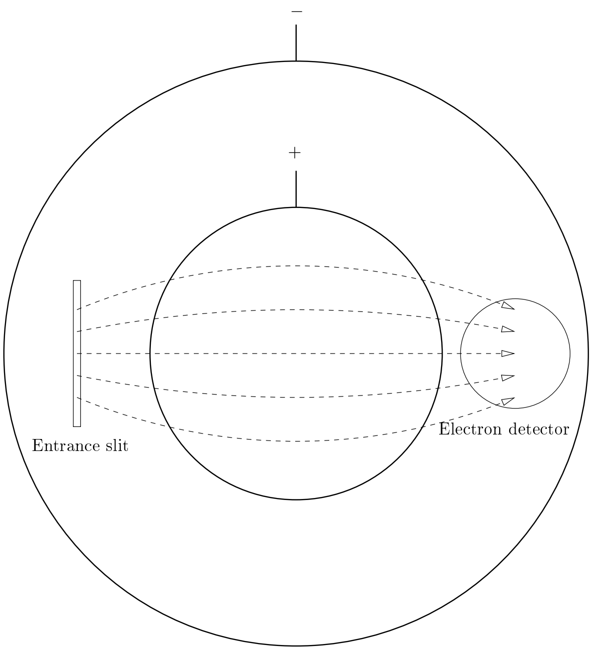

Figure 4.6: Angular dispersion in the hemispherical energy analyser. The electrons enter the analyser through the entrance slit, moving put of the paper. They move in a curved path around the inner sphere and end up hitting the electron detector (going into the paper).

Inside the analyser the electrons follow different paths depending on their kinetic energy and angle of entry. Electrons with a high energy will initially be deflected less than low-energy electrons. Electrons entering at an angle will follow different paths around the inner sphere (see figure 4.6). They will hit the fluorescent screen offset from the center depending on their entry angle.

During angle-resolved (over the ϕ angle) scans the sample is rotated to let different parts of the escaping electrons through, while an automated computer system records a series of evenly-spaced angle-resolved (in the θ angle) images.

Photoemission of valence electrons

Since the electron detector plate in the energy analyser only has a finite size, it is necessary to make a choice between measuring a large range of electron energies simultaneous, or having a good energy resolution. If the analyser is set so electrons from the entire valence band hit the detector simultaneously, the resolution is significantly lowered because all the bands are squeezed into a narrower space. The alternative, the method used to obtain the EDCs in this report, is to vary the pass energy (the energy of electrons hitting the middle of the sensor) across the entire valence band while taking a series of measurements. The measurements can then be layered, yielding an angle-resolved image showing the entire valence band.

The electron detector only shows a small window of the energies and exit angles. By changing the pass energy, this window can be swept across the valence band. It never shows the entire valence band, but all parts of the valence band are measured at some point.

EDCs are often extracted/measured at normal emission, as is also the case here. Although the valence band sweeps are angle-resolved by virtue of the hemispherical analyser, the momentum in the valence band sweeps has not been studied here.

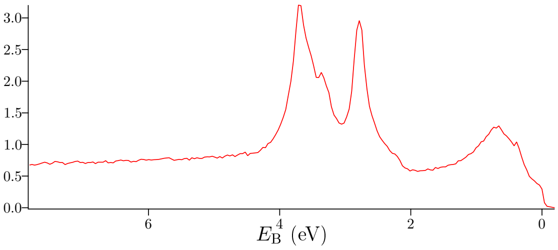

Figure 4.7: Example of an EDC of a Co/Cu(111) sample. The photon energy used was $h\nu = 23$eV. The peak nearest the Fermi level is the 3d-states of the Co and the lower peaks are the 3d-states of Cu.

Chapter 5

Photoelectron Spectroscopy Measurements of surface states and valence band states

The experimental results presented here were acquired at the synchrotron facilities at Århus University, in the laboratory of Professor Philip Hofmann, using the ASTRID storage ring and a UHV system with an angle-resolved hemispherical energy analyser.

All measurements were made over the course of one week using the SGMIII beam line, which was directed into a UHV system with a base pressure of $\sim 10^{-10}$mbar. The Cu(111) crystal used was cleaned with Neon sputtering at 0.75 keV for 20-30 minutes and annealed to 500°C before each preparation.

The metal overlayers were deposited using an E-beam evaporator with multiple pockets, allowing for deposition of Ag immediately after Co deposition. All metal films were deposited at room temperature. After deposition, the sample was moved to a main chamber, where it was put on a helium-cooled manipulator and moved in front of the beam from the storage ring. The sample was turned to face the hemispherical analyser, and measurements began. Sample temperatures during measurement was around 100K when measurement was begun, and around 67K after 30 minutes when the last measurement was finished.

5.1 Data treatment

The experimental setup, as user-friendly as it was, did not deliver the desired information directly. The output files from the setup were the recordings of the energy analyser, which needs some amount of treatment before becoming useable data points. The exact overlayer cpverages were not known either, and some work was done to approximate thhese.

Finding the overlayer coverage

Since the setup used for the ARPES experiments did not include an STM and Auger spectroscopy was relative slow using the installed AES instrument, it was not possible to determine the exact overlayer coverages during the experiments. These had to be calculated later using the measured data, both the surface states and the EDC curves.

Using surface state parameters

The surface states of Ag/Cu(111) have been studied previously, and a shift in energy with increasing coverages has been observed [WWB+04, MKFR+07]. By comparing the onset energies from the Ag/Cu(111) measured here and those in the literature, under the assumption that the measurements in both places are correct, it becomes possible to estimate the deposition rates and coverages of Ag.

Figure 5.1 shows how the deposition rate of the Ag was found. Data points from the literature were plotted along with data points from both preparation series. The coverage of each sample is assumed to be proportional to the deposition time:

$$c_{\mathrm{Ag}} = r_{\mathrm{Ag,i}}\, t_{\mathrm{Ag}}$$

where $r_{\mathrm{Ag,i}}$ is the deposition rate for series 1 and 2. By scaling $r_{\mathrm{Ag,i}}$ to place the measured data points in line with the references, approximate deposition rates were found. By multiplying these with the deposition times from each experiment, the coverage of Ag can be known. The found rates are shown in table 5.2.

Using EDC cross sections

Since the Co/Cu(111) do not show signs of a Co surface state, and the Cu surface state does not shift with Co coverage (discussed later in this chapter), it was not possible to use a similar method for finding the Co deposition rates. Instead these were found by fitting and comparing the areas under the Co d-band peak in the EDCs for a number of Co/Cu(111) to the area under the Ag 4d peaks in Ag/Cu(111) EDCs.

By plotting the total area the Ag d-band peaks in a number of EDCs, a relationship between area and coverage can be found. An initial assumption would be that for equal coverages, the areas should also be equal. This, however, is not the case.

Following from Fermi's golden rule (See equation (4.2)), the probability of an electron being excited by in incoming photon is not constant for all states and photon energies. Fortunately this can be compensated for using *photoionization cross-sections*. These are values representing the relation between areas

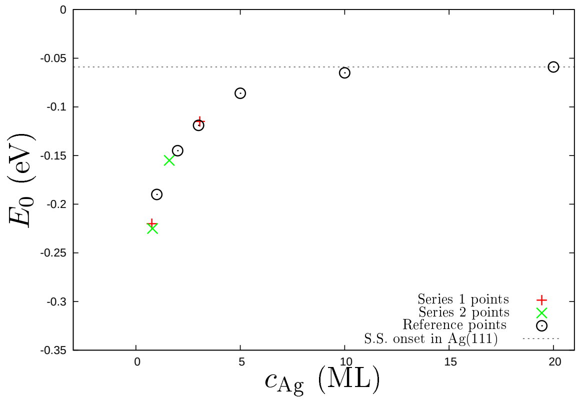

Figure 5.1: Data points used to determine deposition rates for Ag in the two experiment series. The black circles are from [MKFR+07], and were measured using $h\nu = 21.2\text{eV}$. The new measurements were taken at $h\nu = 23\text{eV}$.

under the EDC peaks corresponding to specific electronic states. The assumption regarding the relationship between the areas under Ag and Co d-band peaks now become

$$\frac{A^{n\text{ML},h\nu}_{\text{Ag,4d}}}{\sigma^{h\nu}_{\text{Ag,4d}}} = \frac{A^{n\text{ML},h\nu}_{\text{Co,3d}}}{\sigma^{h\nu}_{\text{Co,3d}}}\,, \tag{5.1}$$

where $A^{n\text{ML},h\nu}_{\text{Ag,4d}}$ and $A^{n\text{ML},h\nu}_{\text{Co,3d}}$ are the total fitted areas under the Ag 4d and Co 3d peaks, respectively, for coverages of nML. $\sigma^{h\nu}_{\text{Ag,4d}}$ and $\sigma^{h\nu}_{\text{Co,3d}}$ are the cross-sections for each state at a specific photon energy.

The cross-sections are tabulated in [YL85] for certain commonly used photon energies, but not for the specific energies used here. To approximate them, the four closest values were fitted with an interpolating line, and the cross-sections were found to be:

$$\begin{array}{ll}
\sigma^{23\text{eV}}_{\text{Ag,4d}} = 19.089\,\text{Mbarn} & \sigma^{32\text{eV}}_{\text{Ag,4d}} = 28.557\,\text{Mbarn} \\
\sigma^{23\text{eV}}_{\text{Cu,3d}} = 7.592\,\text{Mbarn} & \sigma^{32\text{eV}}_{\text{Cu,3d}} = 8.816\,\text{Mbarn} \\
\sigma^{23\text{eV}}_{\text{Co,3d}} = 4.882\,\text{Mbarn} & \sigma^{32\text{eV}}_{\text{Co,3d}} = 6.853\,\text{Mbarn}
\end{array}$$

Table 5.1: Cross-sections for Ag 4d, Cu 3d and Co 3d states. Found by interpolating the four closest points in [YL85].

By normalising the fitted areas of d-bands using cross-sections as in (5.1), plotting the values and finding linear fits, the deposition rates of Co could be found. This method was used on curves taken with 23eV and 32eV, a total of three deposition rate values were found. Two values were found for the second rate, and only one for the first due to a lack of data points. The values are listed in table 5.2.

Deposition rates

In the first version of this report, a different method was used to unite the two sets of experiments with different deposition rates. By comparing the height of the peaks, rather than the area, a scaling factor was found. It was then used to scale the deposition times on one set of experiments to find equivalent deposition times. This method did not take into account the width of the peaks or the difference in photoionization probability.

Using this new method, much more useable results were achieved. With the new method it became possible to find the exact coverages on the samples. With the old method it was not possible to compare the results quantitatively, since only relative coverages could be found using the deposition time alone. However, it should be noted that the rate ratios found using the previous method were not entirely off. The scaling factor for Co was found to be 1.33 using the previous method, and 1.43 using the area and cross-section-based method. For Ag the time-scaling method gave a ratio of 3.76, whereas the new method only gives 2.35.

Metal	Photon energy	Series	Deposition rate
Ag	-	1	$0.0085\frac{\mathrm{ML}}{\mathrm{s}} = 0.51\frac{\mathrm{ML}}{\mathrm{min}}$
Ag	-	2	$0.02\frac{\mathrm{ML}}{\mathrm{s}} = 1.2\frac{\mathrm{ML}}{\mathrm{min}}$
Co	32	1	$0.015\frac{\mathrm{ML}}{\mathrm{s}} = 0.9\frac{\mathrm{ML}}{\mathrm{min}}$
Co	23	2	$0.025\frac{\mathrm{ML}}{\mathrm{s}} = 1.5\frac{\mathrm{ML}}{\mathrm{min}}$
Co	32	2	$0.018\frac{\mathrm{ML}}{\mathrm{s}} = 1.08\frac{\mathrm{ML}}{\mathrm{min}}$

Table 5.2: Deposition rates of silver and cobalt. The deposition rates for silver were found by comparing surface state onsets to literature references, and the cobalt rates were found by comparing the areas under the cobalt 3d peaks to the areas under silver 3d peaks.

For the silver deposition rates and the first cobalt rate, the only value found was used. For the second cobalt rate, an average of the two values was used.

A parameter that was not included in the new model is the close-packing of the individual atoms. Silver has a larger lattice constant than copper or cobalt, and will therefore have fewer electrons in a given state per surface area. This was not taken into account, but it could possibly have been done by a simple scaling of either the Co or Ag peak areas by the difference in density of atoms. The photocurrent has not been included either, as this was not recorded during the experiments. This is not a problem, as long as one assumes that it remained constant during all experiments.

Treatment of ARPES scans

The experimental equipment was relatively straightforward to use. Within minutes of preparing a sample, an image of the surface states is shown on the computer screen, and all data acquisition and most equipment configuration was automated. Most of the data acquisition is controlled by a data treatment program called *Igor Pro*, which has also been used for much of the data treatment.

Each of these acquired images have been treated in the following way:

1. Each image is stored in a separate file, which is loaded into Igor Pro. Here is is run through an algorithm made by PhD-student Marco Bianchi (Århus University), which places the correct scales on the image.
2. The images are initially plotted with intensities in gray-scale, kinetic energies on the vertical axis and emission angle on the horizontal. In order to calculate the effective masses, it is necessary to map the image against wave numbers. To do this mapping without pulling the surface states out of shape, the angular scale must first be centered properly. The surface states are fitted with a parabola, which is used to center the angular axis. The axis is not stretched but merely offset in this step. Rotating the sample in the plane of the entrance slit would also have this effect, however this was difficult to do because of the manipulator design.
3. Once the surface state is properly centered, the image is k-warped[1].
4. We want to know the energies relative to the Fermi level, so the Fermi level is fitted with a Fermi function and the vertical axis is offset as well. The sign is also inverted so the graph now shows binding energies rather than kinetic energies of the emitted electrons.
5. Finally, the state is fitted again with a parabola. This time it is used to calculate the effective mass of an electron in the state and find the exact value of the onset.

In some of the images, the surface states were not fitted and included below. In many cases the surface states were simply not visibly on the images, while in others it was too weak for the fitting algorithms to catch on.

5.2 Valence band states

In addition to measurements of the surface states in the studied systems, valence band photo emission spectra were also recorded for most of the samples.

---

[1] The term “warped” is used here because the conversion from angular to wave numbers is dependent on both the angle and kinetic energy, and the image is stretched in some areas as a result.

These were recorded by letting the hemispherical analyser capture a series of overlapping images covering the valence band. By extracting a narrow portion of this image, one ends up with an *energy distribution curve.*

An EDC shows the distribution of electrons across different energy levels. Since d-bands often play a large role in bonding [HN95], and d-bands are such a visible feature in an EDC, it's not difficult to see that an EDC could potentially give important information about changes in the chemical properties of a surface.

In the systems studied here there are tree groups of peaks, originating with three different d-bands. The surface states can also be seen as smaller peaks near the Fermi level.

- The surface states of Ag and Cu have binding energies around ~ 0.2eV and ~ 0.4eV[2], respectively, and can be seen as a small peak nearest the Fermi level in figure 5.2, up against the Co 3d band.

- The peak with the lowest binding energy is the 3d-band of the Co. It's located close to the Fermi level at ~ 0.8eV. There is only a single peak seen here, unlike Cu and Ag bands which are split into multiple peaks. The d-orbitals in Co are only partially filled with 7 electrons out of 10 possible, which shows in the shape and location of the peak. When trying to fit Lorentzian functions to the Co 3d band, parts of the Lorentzian would some times stick out past the Fermi level.

- Next are the 3d-bands of the Cu, with several peaks in the $2-4$eV range. These are not shifted relative to bulk Cu, since we are effectively measuring bulk Cu. The bands of Ag and Co may be changed as their lattice constants and structures are altered by the lattice mismatch, however these things do not take effects do not take place on a significant scale in the Cu.

- The last states are the 4d-states of Ag. These peaks are the most strongly bound to the sample, and are located in the $4-7$eV range.

The EDCs for the experiments have not been treated in any significant way, except for the cross-sections extracted when finding deposition rates. A selection of the EDCs are presented here. Although the positions of the d-bands are very important in chemical bonding, the TPD-experiments did not yield any quantitative measurements of bonding properties of Co/Cu(111), making any comparisons between the two sets of experiments difficult.

The EDCs for the Ag/Cu(111) systems are shown in figure 5.3. There are only a few EDCs included here, and so it might be too early to conclude anything for the Ag d-bands. However, it's clear that the Cu states are stationary

---

[2] They shift with surface composition, as described below, but are generally in these areas.

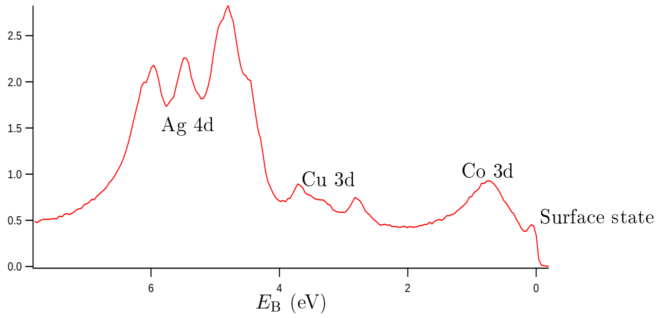

Figure 5.2: Approximate positions of the various valence band peaks. The EDC is taken from a Ag(1.6 ML)/Co(1.9 ML)/Cu(111) sample at $h\nu = 23$eV.

and are not shifted by the Ag overlayers. For lower Ag coverages the Ag 4d peaks are places further apart, and move closer together at higher coverages.

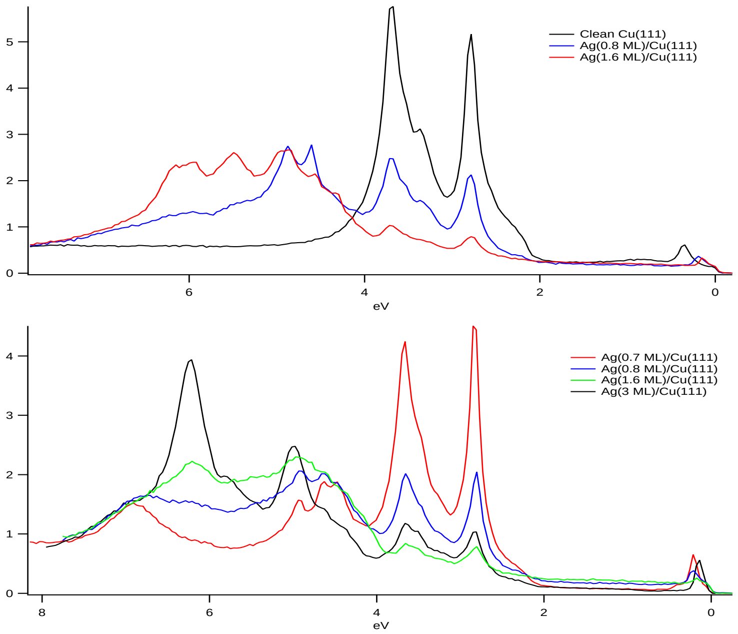

Figure 5.3: EDCs for Ag/Cu(111) systems. The EDCs in the top graph were recorded with a photon energy of $h\nu = 23eV$, and the bottom ones using $h\nu = 32eV$.

There are a few more EDCs for Co/Cu(111) than for Ag/Cu(111), making it easier to see any trends in their positions. As with Ag, the d-bands for Co are also stationary for the coverages used here. Some authors suggest that it might shift with higher coverages[LC98], but the limit for this shift is clearly higher than what has been used here. During pseudomorphic growth the Co is placed closer together, and the electronic overlaps are increased. With higher coverages the Co would eventually relax to its bulk lattice constant, reverting all effects of the pseudomorphic growth.

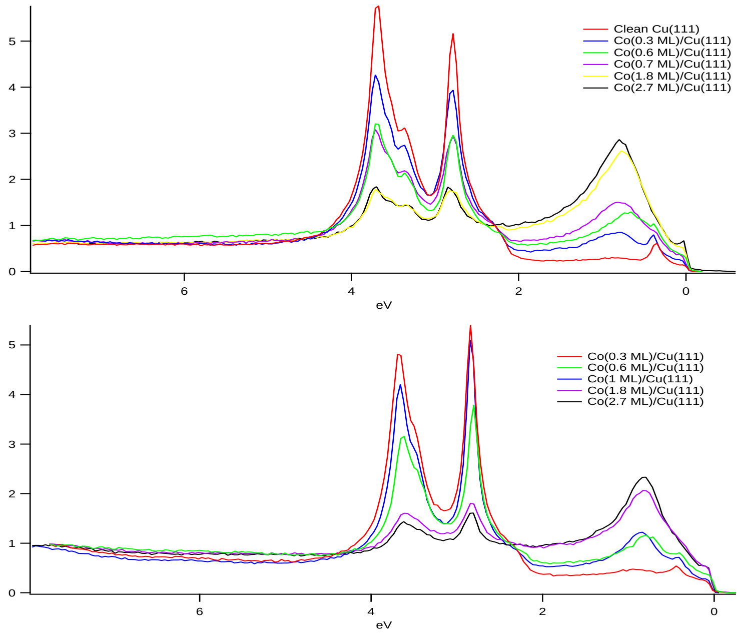

Figure 5.4: EDCs for Co/Cu(111) systems. The EDCs in the top graph were recorded with a photon energy of $h\nu = 23eV$, and the bottom ones using $h\nu = 32eV$.

Finally there are the EDCs for the sandwich Ag/Co/Cu(111) systems. There were made a large number of preparations of these samples, but a number of factors has made it difficult to compare them all. EDCs for the four preparations used earlier are shown in figure 5.5. These preparations all have equal amounts of AG deposited, but the amount of Co underneath was varied.

One could possibly perform more detailed studies of how the peaks grow relative to each other, and how photoelectrons are blocked out by different overlayers, but that is a subject in itself. The only features studied here are the locations of the d-bands.

5.3 Surface state scans

In this section the images of surface states are (finally) shown. The surface states for both Cu(111) and Ag overlayers have been fitted as explained above,

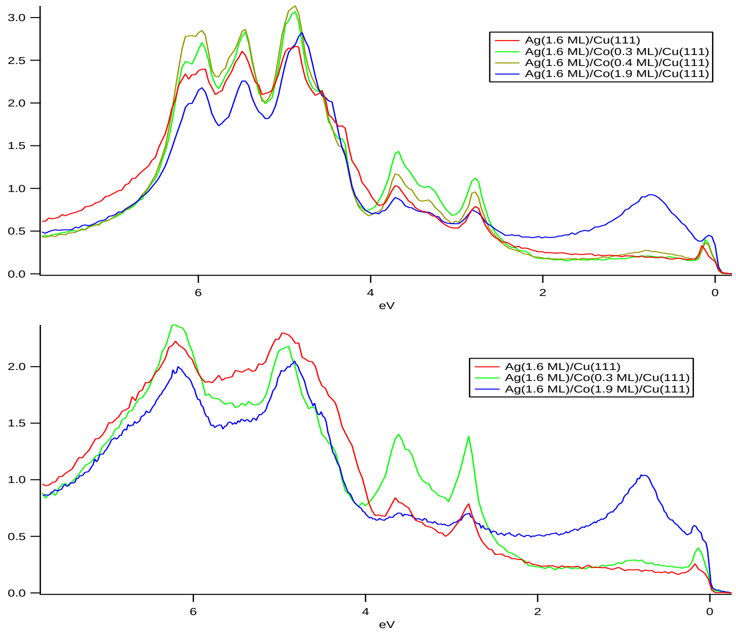

Figure 5.5: EDCs for a selection of the Ag/Co/Cu(111) preparations described earlier. All samples were prepared with identical amounts of Ag (1.6ML) and varying amounts of Co. The EDCs in the top graph were recorded with a photon energy of $h\nu = 23eV$, and the bottom ones using $h\nu = 32eV$.

and the bond energies and effective electron masses have been plotted. The scans are divided into three parts:

- Co/Cu(111) preparations only have the surface state of Cu (the Co surface state is not visible), and the Cu surface state is only visible for lower Co coverages.
- Ag/Cu(111) preparations may have one or both of the surface states. In most of them the Ag coverage has been so high that the Cu surface state has died out, and so only the Ag states are plotted here.
- Finally the sandwich layers, Ag/Co/Cu(111), are plotted. A series with constant Ag coverage and varying Co coverage is plotted.

There are two sets of measurements in each graph. The blue circles are measurements taken at 23eV, and the red squares at 32eV. The "blue" set is generally nicer looking, with clearer tendencies. The "red" set is more irregular. The explanation may be, that the measurements at 23eV were done first, and the ones at 32eV last. During measurement the sample was held at 67K, making it very susceptible to impurities.

Co/Cu(111)

The first system studied consists of cobalt overlayers on a clean Cu(111) substrate. Although silver layers are introduced later, a number of experiments were also carried out without. Figure 5.6 shows the parameters of the surface states in these systems.

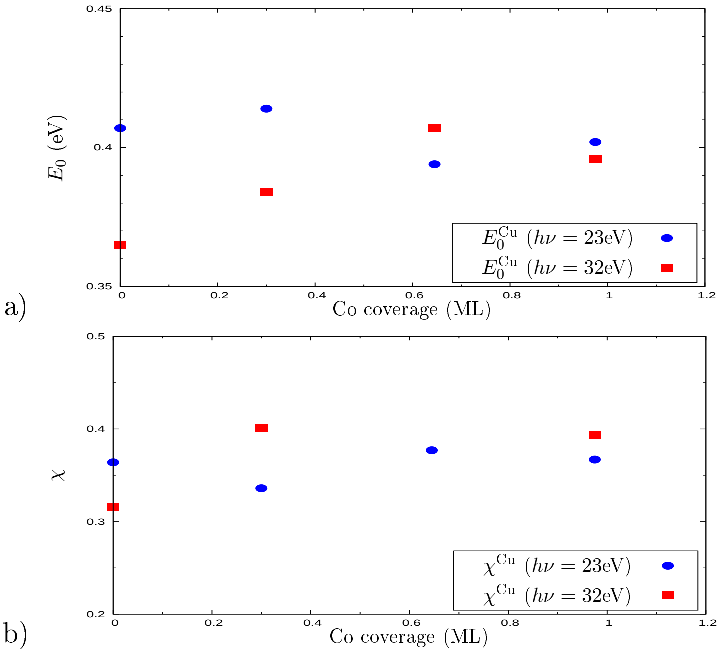

Figure 5.6: **a)** Values of E_0 and **b)** effective fractional masses for the Cu surface state in Co/Cu(111) samples. Both parameters are very stable and do not change with increased Co coverage. The measurements at 32eV were taken last, which could possibly account for the irregularities seen in those points.

Although cobalt does have a surface states of it's own, all surface states found in these systems are those of the copper. The cobalt surface state is not visible. If there is a shift in the energy levels of the Cu states in the Co/Cu(111) systems, it's very small.

The effective masses tell the same story. They're virtually unchanged, and if there's any shift it's too small to register.

Ag/Cu(111)

There were also made experiments with silver directly on the copper surface. Silver, unlike cobalt, gives rise to a surface state of it's own, resulting in two states to be observed. Figure 5.8 shows values of E_0 for the Ag surface states.

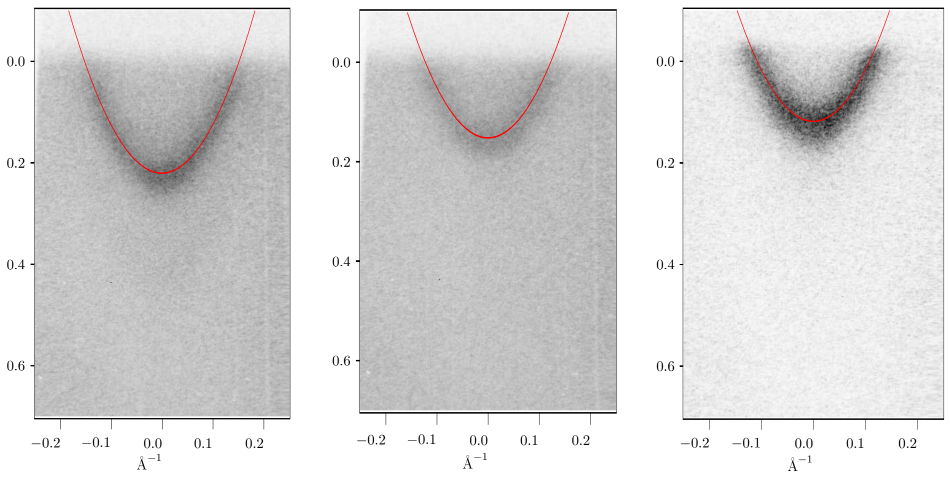

Figure 5.7: Examples of Ag surface states in Ag/Cu(111). The Ag coverages in these images, going from left to right, were 0.8ML, 1.6ML and 3.0ML, respectively.

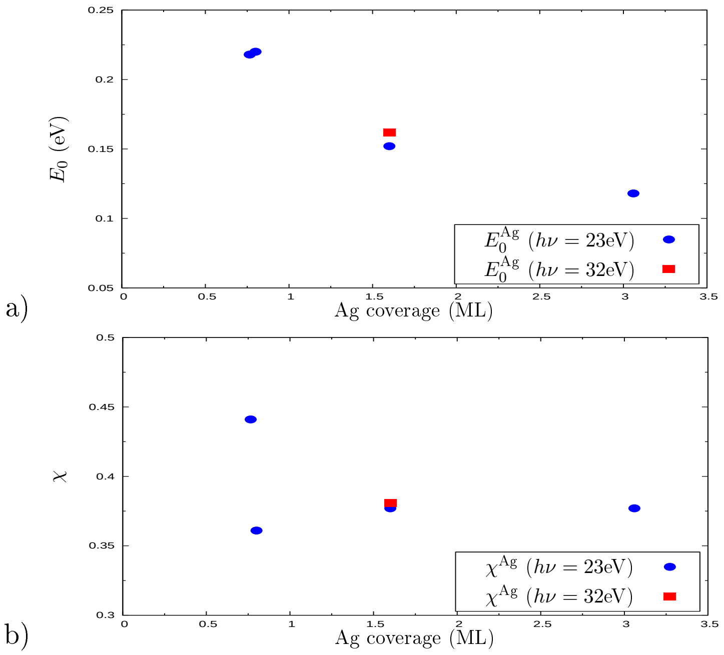

Figure 5.8: **a)** Plotted values of E_0 of the Ag surface state versus Ag coverage. There is a clear decrease in the binding energy of the state with increasing amounts of Ag, even at multiple layers. **b)** The changes in the effective fractional mass, χ, are not as systematic.

In the silver states there is a shift down in the binding energy as more silver is deposited onto the sample, even with multiple layers deposited. This could indicate that surface states are not only affected by steps at the surface, but also steps inside multiple layers.

Ag/Co/Cu(111) sandwich layers

The Ag/Co/Cu(111) sandwich layers were the main system of interest. The original plan behind the ARPES experiments were to look for a modification of the surface states in these structures due to the lattice mismatch induced moire pattern in the silver layer on top. No moire-related splitting was observed, however another effect was seen. It was observed that, when varying the amount of cobalt deposited before the silver layer, the silver surface state would shift in energy.

Figure 5.9 shows three ARPES images. All of the images are of a silver state in an Ag/Co/Cu(111) sample, and all of the samples have been covered with the same amount of silver. The difference between them is in the amount of cobalt underneath, and the effect is a clear down-shift in binding energy.

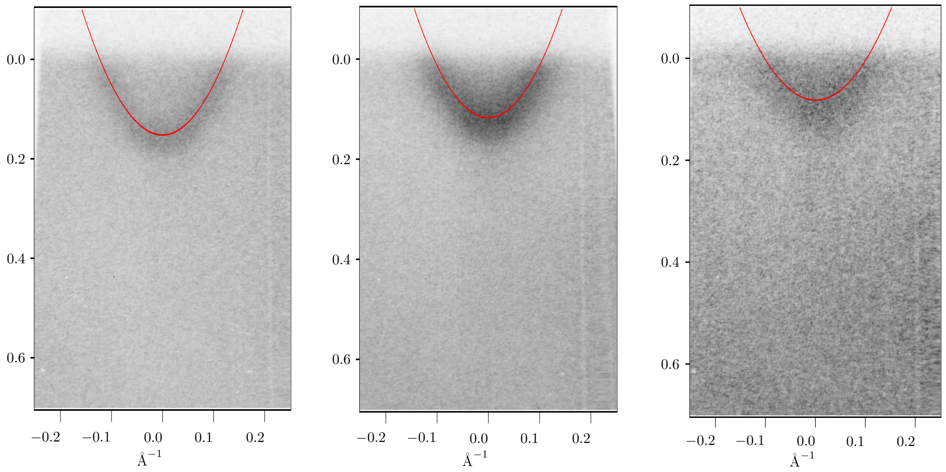

Figure 5.9: Three ARPES images of Ag surface states in Ag/Co/Cu(111) systems with different Co coverages. All samples were prepared with the same dose of silver (1.6 ML) on top of Cu(111) with no or some Co deposited. The Co coverages, from left to right, are 0 ML (clean), 0.3 ML and 0.6 ML. Notice the shift towards the Fermi level as the Co coverage is increased. All images were recorded with a photon energy of $h\nu = 23$eV.

Figure 5.10 shows the values of E_0 for four such samples, measured using two different photon energies. It's obvious that a shift occurs with increasing cobalt coverage, but the last point (1.9 ML of Co) is an outsider. All the

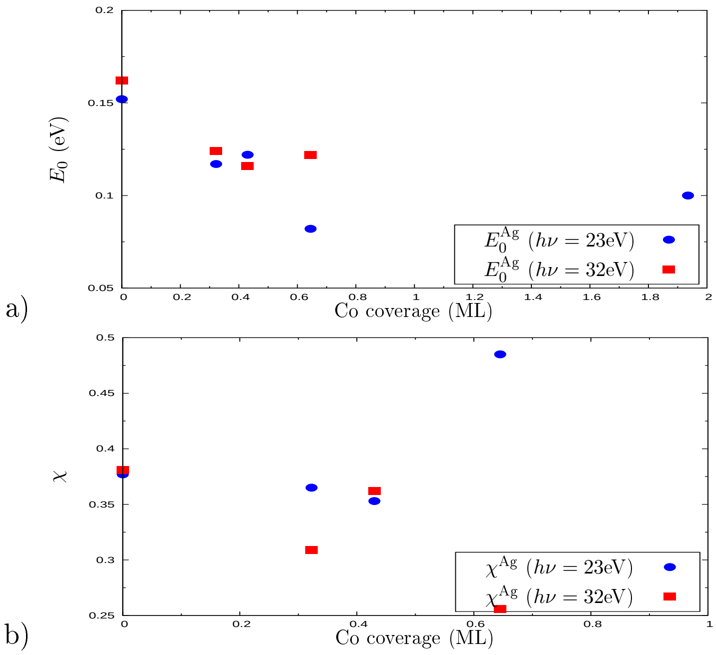

Figure 5.10: **a)** Plotted values of E_0 for the Ag surface state in the Ag/Co/Cu(111) samples. There is a decrease in binding energy as the underlying Co coverage is increased, except for at the last point, where E_0 is at the same level as for lower coverages. If the decrease in energy was constant, the last point would have been much lower.

remaining points have coverages below 1 ML, meaning that the Co forms individual islands of bilayer height. With a coverage of nearly 2 ML, the Cu(111) substrate has been nearly covered by Co, severely limiting the number of bilayer steps in the Ag layer.

5.4 Partial conclusion

Shifts in the binding energy of surface state electrons was observed in Ag surface states in Ag/Cu(111) and Ag/Co/Cu(111) systems, but similar effects were not seen for the Cu surface state.

A possible explanation might be, that while the Ag state is moving in the Ag overlayers, which are disturbed by the underlying steps of either Co islands or Cu(111) steps, the Cu surface state is localized to a substrate. A state moving in the substrate will only feel the disturbances of surface structures from one side, whereas the Ag states in the overlayers are disturbed by both steps below as well as the steps in the Ag overlayer. A cobalt island under a layer of silver will have a larger effect on the states in the silver layer, than it would hav on a copper surface state below it.

There also appears to be some tendency for the effective masses to decrease as the binding energy does, meaning that the intersections of the surface state with the Fermi level are not changed as much as would be expected.

In the Ag/Co/Cu(111) samples, further evidence of step-site interaction was observed. With low coverages of Co in the middle layer, a down-shift in binding energy was observed, however when the Co was covering the sample almost completely, E_0 was at the same level as with low Co coverages. One could imagine that the Co island landscape at this point has become so dense that the holes in the Co layer now serves the same effect as the islands did at first.

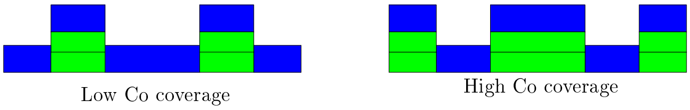

Figure 5.11: Sketch of a possible explanation of why the last point does not follow the same linear decrease as the other points. At low coverages the Ag overlayer is disturbed by protruding Co islands. At high coverages the Co layers cover the sample almost completely with only a few holes through to the Cu(111). The holes act as disturbances in the Ag layer in the same way the Co islands did.

Chapter 6

Surface-molecule bonds

In this chapter, some of the mechanisms behind chemical bonding are discussed. The starting point will be the electronic states of the atoms and molecules involved, and some bonding mechanisms will be explained in terms of these.

The systems studied in the experimental sections are overlayer systems, and so their chemical properties will also be mentioned. Small amounts of transition metals on noble surfaces have been shown to have chemical properties different from those of the bulk materials. The origin and effect of these changes are discussed.

6.1 Chemical bonding from an electronic perspective

The focus of this chapter is to explore and describe the bonding between molecules and surfaces in terms of the electrons and their states. In short, chemical bonding is the interaction between overlapping atomic and molecular orbitals. The total energy of a system may be reduced by partially overlapping certain orbitals as this can cause the orbitals to split and allow for electrons to move to states with lower energies. Since all systems tend towards the lowest possible energy, this can under certain circumstances result in atoms or molecules forming bonds. The models for bonding described on the following pages will be based on this view.

Diatomic molecules

In order to describe the chemical bonding between molecules and a surface, it is necessary to first examine the bonds between individual atoms. Although the bond between a pair of atoms is considerably simpler than that between a molecule and a surface, it can still give important insight into chemical bonding in general.

As written above, chemical bonding can be described as the overlapping of atomic orbitals. First we consider a simple diatomic molecule with only a single electron. When the two atoms are separated and are not interacting we label the wave functions ψ_1 and ψ_2 respectively. The energies of these states are

$$\begin{aligned} \epsilon_1 &=< \psi_1|H|\psi_1 > \\ \epsilon_2 &=< \psi_2|H|\psi_2 > , \end{aligned}$$

with H being the Hamiltonian.

As the two atoms are brought closer, we will calculate a new wave function for one of the electrons as a linear combination of the atomic wave functions.

$$\psi = c_1\,\psi_1 + c_2\,\psi_2$$

By the principle of least action, the constants c_1 and c_2 must be chosen to minimise the energy of ψ. The energy is

$$E =< \psi|H|\psi > \ .$$

In this case the Hamiltonian is

$$H = -\frac{\hbar^2}{2\,m_e}\lambda^2 + \frac{1}{4\,\pi\,\epsilon_0}\left(-\frac{e^2\,Z_1}{r_1} - \frac{e^2\,Z_2}{r_2} + \frac{e^2\,Z_1\,Z_2}{R}\right) ,$$

where m_e is the mass of the electron, r_1 and r_2 are the distances from the atom's nuclei to a given location of an electron wave function and Z_1 and Z_2 are the atomic numbers of the atoms. R is the distance between the nuclei, that is, . the bond length.

The energy of the system can be minimised by solving the secular equations[Dah05]:

$$\sum_i c_i\,(H_{i\,k} - E\,S_{i\,k}) = 0$$

These equations can be put into matrix form. ψ_1 and ψ_2 are assumed normalised.

$$\begin{bmatrix} \epsilon_1' - E & \eta - E\,S \\ \eta - E\,S & \epsilon_2' - E \end{bmatrix} \begin{bmatrix} c_1 \\ c_2 \end{bmatrix} = \begin{bmatrix} 0 \\ 0 \end{bmatrix} ,$$

with

$$\epsilon_1' =< \psi_1|H|\psi_1 > , \tag{6.1}$$

$$\epsilon_2' =< \psi_2|H|\psi_2 > , \tag{6.2}$$

$$\eta = H_{1\,2} = H_{2\,1} =< \psi_1|H|\psi_2 > , \text{and} \tag{6.3}$$

$$S = S_{1\,2} = S_{2\,1} =< \psi_1|\psi_2 > \ . \tag{6.4}$$

If this system is to have non-trivial solutions, the determinant must vanish.

$$\begin{vmatrix} \epsilon_1' - E & \eta - E\,S \\ \eta - E\,S & \epsilon_2' - E \end{vmatrix} = 0$$

Some re-ordering leads to:

$$E = \frac{-2\,S\,\eta + \epsilon_1' + \epsilon_2' \pm \sqrt{\left(2\,S\,\eta - \epsilon_1' - \epsilon_2'\right)^2 - 4\,\left(1 - S^2\right)\,\left(\epsilon_1'\,\epsilon_2' - \eta^2\right)}}{2\,(1 - S^2)}$$

A common approximation for this problem is to assume a small overlap and removing all terms containing S^2. More rewriting yields

$$\begin{aligned} E &= \frac{-2\,S\,\eta + \epsilon_1' + \epsilon_2' \pm \sqrt{-4\,\left(\epsilon_1' + \epsilon_2'\right)\,S\,\eta + 4\,\eta^2 + \left(\epsilon_1' - \epsilon_2'\right)^2}}{2} && (6.5) \\ &= \frac{\epsilon_1' + \epsilon_2'}{2} \pm \sqrt{-\left(\epsilon_1' + \epsilon_2'\right)\,S\,\eta + \eta^2 + \frac{\left(\epsilon_1' - \epsilon_2'\right)^2}{4}} - S\,\eta\,. && (6.6) \end{aligned}$$

From this it is clear that the electron can exist in two orbitals when the atoms are bound. In the first term we have simply the average of the two one-atom orbitals. The two orbitals then appear as the second energy term is either added or subtracted. Finally, both orbitals are shifted slightly up by the last term, $-S\,\eta$. Since S is positive and η is negative, the final term is a repulsive term, moving both orbitals higher and thus reducing the bond strength.

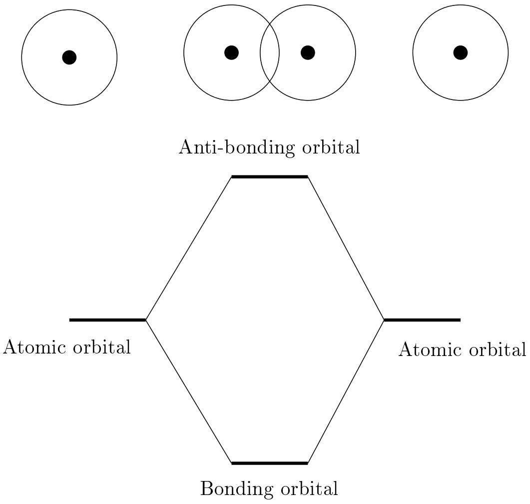

Figure 6.1: Single states of isolated atoms and bonding/antibonding orbitals for overlapping atoms in a diatomic molecule.

These orbitals are usually called bonding and anti-bonding orbitals, respectively, since one orbital will lead to a stable molecule and the other will lead to a breaking of the bond. The bonding orbital, with the lowest energy of the two, resides below the average of the one-atom energy levels. If the electron in question is occupying this orbital, the two atoms can achieve a lower energy than before. If this bonding orbital did not exist and only the anti-bonding orbital was available, the molecule would quickly dissociate since the energy of the bound molecule would be higher than that of the individual atoms.

Atomic chemisorbtion

Based on the previously described model for molecular bonding, a model for the adsorption of an atom onto a surface will now be presented. The principle behind the following is essentially the same as before: The wave functions of the electrons in the bound state of the system will be described as a linear combination of the orbitals in the non-bound system. This concept is often abbreviated LCAO (Linear Combination of Atomic Orbitals) and is commonly used in tight-binding calculations. The approach taken in the following could be seen as a variant of the tight-binding calculations used to find the energy levels of atomic orbitals inside a bulk material.

The big difference between the case of a diatomic bond and atomic adsorption is that whereas a single atom was assumed to have only a single atomic orbital (in the simplified model used here), a surface will have continuous bands of states [CN03].

The origin of the broad bands in the bulk material is very similar to the splitting of the wave functions in the diatomic molecule. Just as the overlapping of two atoms in a molecule gives rise to two new energy levels, the overlapping of many atoms in a solid will also lead to a splitting of the energy levels. However, due to the vast number of atoms in solids and the many overlaps, the energy levels of a solid are not split into a finite number of states but rather a continuum of states.

As with the diatomic molecules, the amount of splitting (the distance from the lowest to the highest state in the band) is very much dependent on both the magnitude of the overlap and energy terms. Because not all orbital types overlap to the same degree the resulting bands in the solids may take on many different shapes. In general there are two types of bands, sp- and d-bands[1]. The overlaps between s- and p-orbitals are larger than between d-orbitals and the resulting bands are therefore much wider, but also have a lower density of states. The d-orbitals have weak interaction in comparison, resulting in a much narrower band with a higher DOS [CN03].

The calculations performed for a diatomic molecule can also be used as an extremely simplified model of atomic (and molecular) chemisorption on a solid. Here, one would make the assumption that only one electron from the atom (or molecule) interacts with a single state in the solid. The same assumption

---

[1] Surface states are also a form of electronic bands but they are not a result of atomic orbital overlaps. These states will be treated in chapter 3.

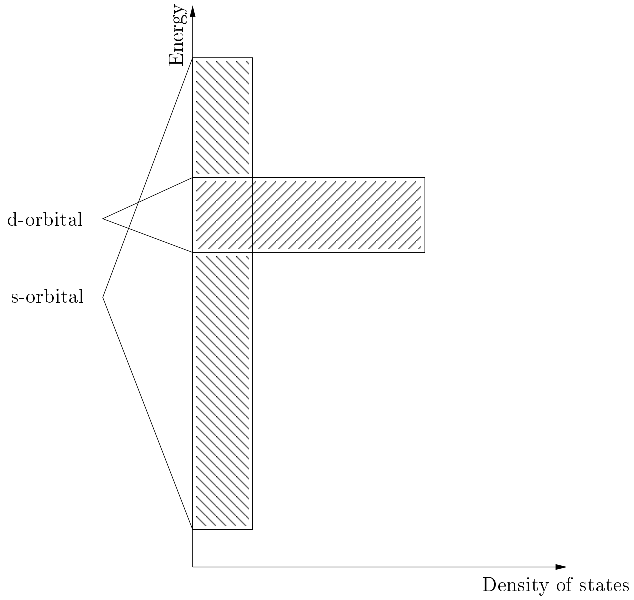

Figure 6.2: Simplified representation of the bands resulting from sp- and d-band overlaps. The d-orbitals have weaker interaction and therefore become a narrower band, but with higher density of states. The relatively weak sp-interactions result in a broad band with a low DOS.

is made for diatomic molecules, however here the assumption has more justification. In molecular bonding there are usually a relatively few electrons that contribute to the bonding to a much greater extent than the others. It is not unjustified to make predictions based on the strongest interactions of these main contributers while discounting the lesser influences. This assumption, however, can not be applied to adsorption onto surfaces because, although surfaces also have some orbitals that may contribute more to bonding than others, these bands of bonding contributors are not single states and can not be treated as such.

The Newns-Anderson model

As with the bonding between atoms, the adsorption of atoms onto a surface will be modelled as linear combination of the electronic states of each component. In this case those states would be the single-energy orbitals of the electron and the broad, continuous bands in the solid. This approach for a molecule or atom bonding to a surface is often called the *Newns-Anderson model*[HN91].

Consider an atom as before, with only a single electro in a state ϕ_a. Now, whereas before the bonds between atoms were examined, the atom will now interact with a solid with continuous bands of states rather than the single states of an individual atom. As before the goal is to determine a wave function for the system in the chemisorbed state. A linear combination of the involved wave functions can be expressed as

$$\Psi_i = c_{a\,i}\,\phi_a + \sum_k c_{k\,i}\,\psi_k \ ,$$

where ψ_k are a basis for the states of the surface.

Finding a solution to this problem can be quite a feat. The large (near infinite) number of substrate states makes it impossible to find a solution like that in the previous section. Instead is can be solved using density functional theory, but that will not be included here.

It should be noted that, even though no solution is presented here, the idea behind this treatment of atomic adsorption is not much different from the treatment of diatomic molecules. In both cases the states of the final system are considered to be combinations of the overlapping states of each component.

Molecular chemisorbtion

With atomic adsorption discussed, only molecular adsorption remains to be mentioned. Molecular adsorption is treated in much the same way as atomic adsorption, with only few differences.

In the preceding section the state of an atom adsorbed onto a surface was described as a linear combination of the isolated states of the atom and the surface. The same can be done for molecules, but instead of using the orbitals of the atoms in the molecule, the molecular orbitals (as described in the section on diatomic molecules) are used.

It is important to note that these molecular orbitals most likely are not the same as those in the isolated molecule. When describing a diatomic molecule with only a single electron, the coefficients of the linear combination were chosen to minimise the energy. With the introduction of d- and sp-bands of the surface, the molecular orbitals may change to a more favourable combination of orbitals. Furthermore, the atomic orbitals themselves may shift to new energy levels. They may also be “bent” out of shape.

When considering molecular adsorption (and atomic as well) it is not always sufficient to consider only the occupied states of the adsorbate. If the Fermi level of the adsorbant can be higher than the HOMO (Highest Occupied Molecular Orbital), it is also necessary to include the LUMO (Lowest Unoccupied Molecular Orbital), since previously unoccupied states may also become occupied if the orbitals are shifted below the Fermi level.

The assumption that only a single electron is involved in the bonding is, of course, also a big simplification. While this model may suffice to describe a H_2 molecule, it is insufficient for other molecules. Higher elements have more electrons, all of which interact with each other. In reality all electrons are involved, some more than others.

For bonding with transition metals, such as cobalt, it is not uncommon to disregard the s- and p-orbitals because of their relatively small contributions to bonding. In these cases the bonding is dominated by the interactions of the d-bands [SL10].

The sp-bands are very broad due to a strong interaction between orbitals. This strong interaction also affects the orbitals of an adsorbed molecule, leading to a broadening of the molecular orbitals into bands. The d-bands have much higher intensities than the sp-bands and are also localised to a relatively small energy interval. Because of this they act much like single states in the sense that the splitting of the bands during adsorption is similar to that seen in atom-atom bonding. That is, the orbitals of an adsorbed molecule are not only split into multiple new states, but may also be broadened by the interaction with the sp-band.

There are of course many other cases of chemical bonding and interaction, including dissociation, reactions and interactions between adsorbed molecules and atoms, and self-assembly of larger molecules. These cases are not discussed here.

6.2 Differences between bonding on overlayers and bulk materials

By depositing materials in the monolayer range onto a substrate, the properties of the deposited material can change due to the loss of many of the interactions found in bulk materials. A common occurrence when studying overlayer systems is a shift in the energy levels of the electronic states relative to bulk materials. Since the bonding properties of materials are dependent on their electronic states, a shift in such states can also lead to a shift in bond energies and reactive properties.

One cause for the changes in electronic properties is the change of the lattice constant due to pseudomorphic growth, which increases or decreases the overlap between the orbitals [RHS$^+$97]. Another method is a transport of electrons from the substrate to the overlayers. The substrates used here (Cu, Ag and Au) all have a higher degree of filling in their valence bands than Co, and as a result some of the substrate electrons may jump to unoccupied states in the overlayers with lower energies [RG92].

In the case of cobalt grown pseudomophically on a Cu(111) surface, there is a shift up in the energy levels of the d-bands. During deposition onto the Cu(111) surface the cobalt is stretched to have the nearly the same nearest-neighbor distance as the Cu(111) surface, which reduces the overlaps between the d-states. The narrowing of the d-band will cause it to shift to a new energy level in order to preserve the same degree of band filling [RHS$^+$97].

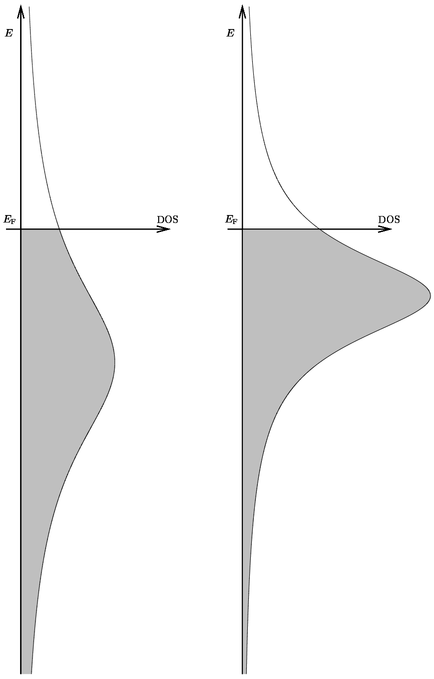

Figure 6.3: A narrowing of the d-band may cause a shift towards the fermi level to preserve the same degree of filling.

Chapter 7

Temperature programmed desorption

As said earlier, the original plan for this project was to study chemical bonds between CO and cobalt overlayers on noble metals using *temperature programmed desorption*. The principle behind TPD is to heat a sample, with some amount of a gas adsorbed onto it, along a pre-set heating ramp. While doing this the partial pressure of one or more desorbed species is recorded and plotted against the sample temperature. By analysing one or more of these desorption curves, it is possible to find information regarding desorption energies and adsorption states [Red62], as well as the order of desorption and activation energies [HK84, LK74].

7.1 Theory of TPD and data treatment

The most common temperature ramp is a linear one

$$T\,(t) = T_0 + \beta\; t\;, \tag{7.1}$$

where t_0 is the initial temperature an β is the heating rate measured in K s^{-1}. It's possible to use different heating schemes, but a linear ramp is one of the easiest to analyse.

Consider a sample with an amount of gas adsorbed. There will always be some degree of desorption from the surface, depending on the temperature. The rate of desorption is described by [Lüt01]

$$v = -\frac{d\theta}{dt} = v_0\; f\,(\theta)\;\, e^{-\frac{E_{\text{des}}}{RT}}\;, \tag{7.2}$$

where $f\,(\theta)$ is an occupation factor, which describes the probability of a given adsorption site of being occupied. E_{des} is the desorption energy. E_{des} includes both the activation energy and the bond energy, and does not yield the bond energy directly. Referer til aktiveringsenergi i bindingsafsnit R is the ideal gas constant og v_0 is an "attempt factor", the rate at which the adsorbed species vibrates perpendicular to the surface. This is the rate of attempts made at overcoming the activation barrier. Equation (7.2) is an empirical expression based on the Arrhenius formula.

v_0 and E_{des} are used as constants here. In reality they can also depend on the degree of coverage. For example, if the adsorbed species attract each other on the surface, they will be les likely to desorb at a given temperature. In this case the atoms would nucleate into islands on the surface. If the atoms repel each other, they would spread themselved out over the surface.

The overall shape of a desorption curve can be deduced from (7.2). The exponential function will result in an exponential-like growth on the rising side of the curve, but when the adsorbed gas is depleted, the desorption rate will drop rapidly. Calculated examples of this can be seen in figure 7.1.

For a first order desorption proess without dissocoation, ie. where the adsorbed species are either individual atoms or molecules that stay "in one piece" during adsorption, the occupation factor can be assumed to be equal to the coverage. For higher order processes it is still often assumed that [Lüt01]

$$f(\theta) = \theta^n \ ,$$

where n is the order. This assumption will be used from here on.

One of the unknown parameters is the degree of covarage, θ. For processes with $n \geq 2$ it's necessary to know this. The absolute coverage can be difficult to find. One method would be to dose a specific amount of gas onto the sample and then measure the coverage using AES. It is also possible to adsorb a different gas, for which the coverage is known given a certain dose, and then compare the area under the desorption curve to the area under the curve in the system studied. The area under the desorption curve is proportional to the coverage at the beginning of the experiment, and allows for such a comparison if the starting temperature, heating rate and experimental setups are identical.

For many gasses and surfaces the order of desorption is known in advance, but in some cases the order can be unknown. First order desorption can be recognised by simply looking at a set of desorption curves with different initial coverages, θ_0, but second and higher order processes are more difficult to separate. The desorption peaks in higher order processes will shift towards lower temperatures with increasing θ_0.

One of the most interesting parameters is the desorption energy. Using the method described by Redhead [Red62], this can be found using the peak positions of a set of desorption curves. At the top of a desorption peak we know that

$$\frac{dp}{dT} = 0 = \frac{d}{dT}\left(v_0 \, \theta_m^n \, e^{-\frac{E_{\text{des}}}{R\,T_m}} \right) \ .$$

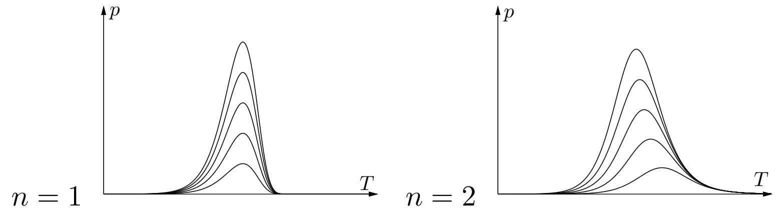

Figure 7.1: Sketches of TPD-spectra with varying initial coverages. For first order ($n = 1$) all peaks are located at the same temperature, but for $n \geq 2$ they shift down in temperature with increasing θ_0. Calculated from (7.2) using an RK4 algorithm.

By differentiating the right equality with respect to T again we get

$$v_0\, e^{-\frac{E_{\text{des}}}{RT}} \left(n\, \theta_m^{n-1} \left. \frac{d\theta}{dT} \right|_{T=T_m} + \theta_m^n \frac{E_{\text{des}}}{RT_m^2} \right) = 0 \ ,$$

where θ_m and T_m are the coverage and temperature at the peak. The two factors outside the parenthesis are never zero, so therefore the contents of the parenthesis must be.

$$n \left. \frac{d\theta}{dT} \right|_{T=T_m} = -\theta_m \frac{E_{\text{des}}}{RT_m^2}$$

Assuming a linear temperature ramp, we can substitute $dT = \beta dt$. Reqriting gives:

$$\begin{aligned} \frac{n}{\beta} \left. \frac{d\theta}{dt} \right|_{T=T_m} &= -\theta_m \frac{E_{\text{des}}}{RT_m^2} \\ \frac{n}{\beta} v_0 \theta_m^{n-1} e^{-\frac{E_{\text{des}}}{R\,T_m}} &= \frac{E_{\text{des}}}{RT_m^2} \\ \frac{T_m^2 \theta_m^{n-1}}{\beta} \frac{n\, v_0\, R}{E_{\text{des}}} &= e^{\frac{E_{\text{des}}}{R\,T_m}} \\ \ln\left(\frac{T_m^2 \theta_m^{n-1}}{\beta} \right) + \ln\left(\frac{n\, v_0\, R}{E_{\text{des}}} \right) &= \frac{E_{\text{des}}}{R\,T_m} \\ \ln\left(\frac{T_m^2 \theta_m^{n-1}}{\beta} \right) &= \frac{E_{\text{des}}}{R\,T_m} + \ln\left(\frac{E_{\text{des}}}{n\, v_0\, R} \right) \end{aligned}$$

By plotting the peak positions of a number of desorption curves as $\left(T_m^{-1}, \ln\left(T_m^2 \theta_m^{n-1} \beta^{-1}\right)\right)$ and fitting a straight line, the desorption energy can be found as

$$E_{\text{des}} = a\, R \ ,$$

where a is the slope of the fitted line.

It is necessary to know θ for $n \geq 2$, but for first order desorption the expression can be reduced to

$$\ln\left(\frac{T_m^2}{\beta}\right) = \frac{E_{\text{des}}}{RT_m} + \ln\left(\frac{E_{\text{des}}}{v_0 R}\right) ,$$

such that knowledge of the coverage is no longer needed. This can also be seen in figure 7.1, where the peaks of first order desorption do not move when the initial coverage is changed.

7.2 Experimental setup

The TPD experiments performed for this project were done in a UHV system with a base pressure of $\sim 10^{-10}$ mbar. The system had a preparation chamber and an analysis chamber, however the preparation chamber was also used for TPD. The preparetion chamber was equipped with a sputtering gun, a sample maniuplator with heating and cooling elements, an e-beam evaporator for metal deposition and a leak valve for dosing gas.

The preparation chamber also had a *quadropole mass spectrometer* which was used to measure the partial pressure of desorbed gasses during the experiments. The temperature was measured using a thermocouple (K-type) on the sample manipulator. Since the temepratur was measured on the manipulator and not the sample itself, there was a difference between the measured temperature and the actual sample temperature. An attempted was made at accounting for this by placing a second thermocouple on a sample plate on the manipulator, and measuring both temperatures during linear heating ramps. The relationship between them was later used to convert the measured temperature to the expected actual sample temperature.

The experimental setup is shown in figure 7.2. The sample is heated by a resistive heating element (tungsten wire), which is powered by an external power supply (*Delta Elektronika 7020-D*). The power supply is controlled by a *Eurotherm 3508*) temperature controller, which is connected to the thermocouple. The Eurotherm controlled the temperature using a PID[1] control algorithm. The partial pressure of desorbed gasses in the chamber were measured by a *Microvision Plus* QMS.

Furthermore, the sample manipulator was equipped with a cooling element, which allowed for the sample to be cooled to less than 150 K prior to the experiment. N_2 gas was passed through a copper coil submerged in liquid nitrogen. The cooled gas was then passed into the cooling element inside the chamber.

Both the QMS and Eurotherm were connected to a computer, which recorded both data sets simultaneously. Data recording was done using a purpose-built

---

[1] Proportional-Integral-Derivative

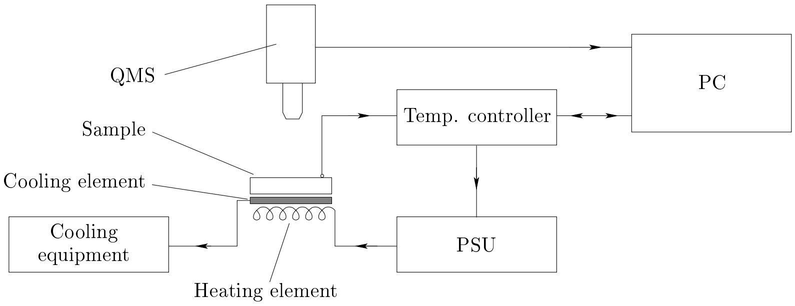

Figure 7.2: Experimental setup for TPD. The sample temperature is measured using a K-type thermocouple and a Eurotherm 3508 instrument, which also controls the power supply for the heating element. The desorbed molecules are detected by a quadropole mass spectrometer. The cooling element can be used before the experiments to lower the starting temperature and increase the temperature range for the experiment.

program made with the *LabVIEW* programming language. The program used drivers from MKS Instruments, the manufacturer of the QMS.

Procedure

Before each experiment the sample was cleaned by repeated cycles of sputtering with Ne^+ ions and annealing to 500°C. The Co overlayers were deposited from an e-beam evaporator at room temperature. After deposition, the sample was transferred to the analysis chamber where the coverage was determined using an STM. Afterwards the sample was moved back to the preparation chamber and CO was dosed. The dosage was varied between 1L and 20L.

After dosage, the sample was removed from the manipulator and the heating filament was degassed for a short time to reduce the degassing peak at the beginning of each experiment. The sample was removed to prevent it from receiving heat during the degassing. The manipulator temperature rose only by a few degrees during the degassing.

After degassing the sample was returned to the manipulator, and the TPD was begun. The sample was heated at a rate of $1\frac{\mathrm{K}}{\mathrm{s}}$.

7.3 Results

All of the results in the following were obThe TPD experiments were carried out using cobalt overlayers on three different substrates. The original focus of the project was to examine if the moire pattern seen in Co/Ag(111) would have an effect on adsorption of CO. Co/Cu(111) was studied as a reference, since no moire pattern is seen here.

TPD of CO from Co/Cu(111)

The results from the experiments using Co/Cu(111) are shown in figures 7.3 and 7.4. Besides desorption of CO from the sample, there was also desorption from the heating filement (rapid degassing when it was turned on) and from the manipulator.

To get a measurement of the noise signal coming from the manipulator, an experiment was made where no gas was dosed onto the sample. The sample was prepared as usual with sputtering, annealing and Co deposition (to ensure than the amounts of Co on the manipulator were the same as usual). The sample was then moved to the adjacent analysis chamber (base pressure of $\sim 10^{-11}$mbar) while the manipulator was dosed with 5L of CO. After the pressure in the prearation chamber had dropped, the sample was moved back to the manipulator and the TPD was carried out as usual. This experiment still showed a desorption peak even though no gas was adsorbed onto the Co islands on the sample.

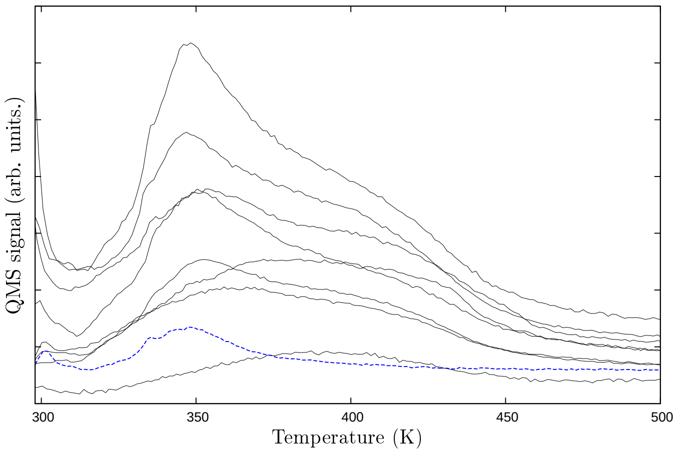

Figure 7.3: Experimental data for TPD of CO from Co/Cu(111). In all experiments the CO was dosed at room temperature. The blue dotted line shows a measurement of the desorption from the manipulator alone. All QMS signals have been scaled relative to their coverage of Co.

Larsen and Chorkendorff has also performed TPD of CO from Co/Cu(111) with a much lower starting temperature [LC98], which also show a desorption peak in the location seen here. In an attempt to replicate their results, an experiment was performed using the sample cooling equipment. In the reference data there are, for high Co coverages, a single peak around 375K. This is desorption from the deposited Co. For lower coverages the highest peak disappears and is replaced by two closely positioned peaks at 125K and $\sim$ 160K, originating from CO desorption from the exposed copper substrate.

For coverages in the 25% to 50% coverage region both features are visible. A Co/Cu(111) sample was prepared with a Co coverage of ∼ 36% by area and cooled to −156°C (∼ 117K). After cooling, 20L of CO was dosed to saturate the adsorption sites. The sample was heated to 573K at an approximate rate of $1\frac{\mathrm{K}}{\mathrm{s}}$. The resulting desorption curve can be seen in figure 7.4 (red broken line) on top of the original data from [LC98].

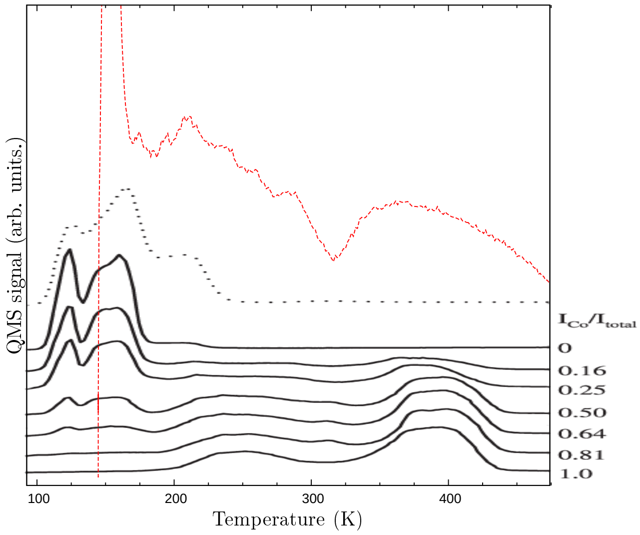

Figure 7.4: TPD of CO from Co/Cu(111). The solid black lines are from [LC98], and the broken red line shows an attempt at replicating the results. Auger intensities are written to the right of the black lines.

There are two main peaks, in addition to the large degassing peak at the beginning of the experiment, in the measured data. The first signal peak streches from 175K to 300K, and the second from 325K to 450K. The higher of the two peaks is located at the same temperature as the reference, however that is not the case for the lower peak. This experiment was begun at a higher temperature than the reference, which may be the cause of the lower peak being located at a higher temperature.

The peaks measured here are very wide and unshapely, whereas the peaks in the reference data are much narrower and easier to differentiate. Considering that the pressure is measured in the entire chamber, it is not unreasonable to think that the same desorption process has taken place both here and in the experiments of Larsen et al., and that the desorption peaks have simply been stretched along the temperature axis due to slow pumping speeds at low pressures.

TPD of CO from Co/Ag(111) and Co/Au(111)

A few experiments were also carried out using Ag(111) and Au(111) substrates. With these substrates no desorption peaks were seen besides the one also found in the noise reference. These experiments were performed in the temperature range from RT to 523K, however some were continued up to 673K to look for desorption peaks at higher temperatures. No desorption peaks were seen using either substrate, indicating that the bond energies for CO adsorption is somewhat lower in these cases than in the Co/Cu(111) experiments.

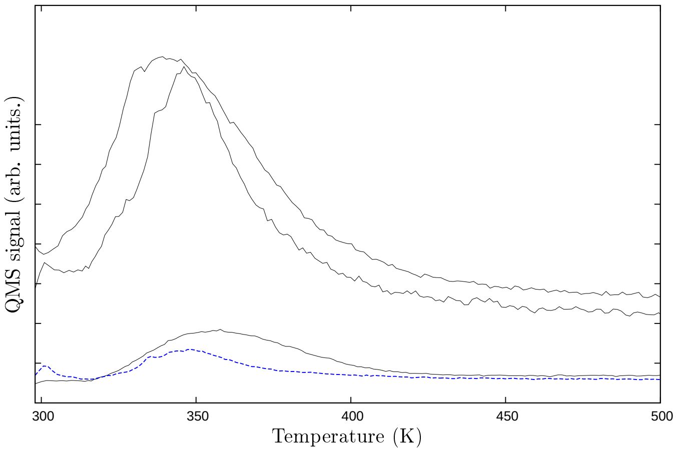

Figure 7.5: TPD spectra of CO from Co/Ag(111) structures. Here the only desorption peak seen is that of the manipulator. The dotted blue line is a reference obtained by running a TPD experiment with no gas on the sample.

TPD experiments with starting temperatures below RT were not carried out due to problems with the cooling equipment.

7.4 Discussion

The results shown above are not quite of the same quality as those found in the litterature, which was the cause for the change of subject.

The peaks in the experiments shown here are very wide and are difficult to analyse. In the experiments of other authors there is significantly less noise than here, and the degassing peaks from the filaments are not seen.

The most prominent source of error is the pressure measurements. The QMS was simply mounted on the chamber, and measured the partial pressure desorbed from all parts of the setup including the sample plate the crystal was attached to, the filament and the sample manipulator. In more advanced setups the QMS is mounted inside a pipe with a narrow opening at the end.

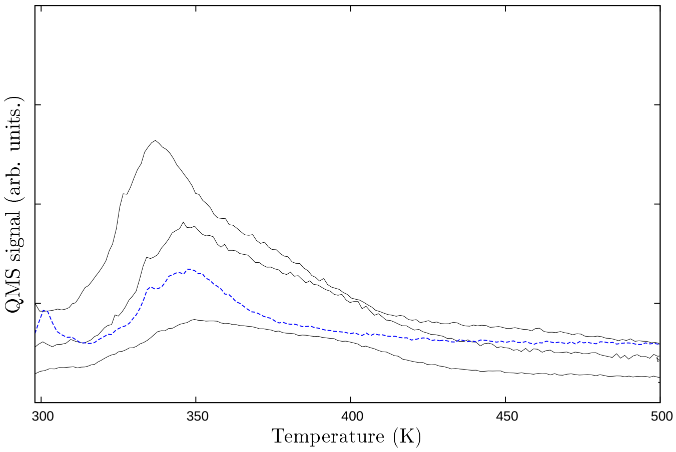

Figure 7.6: TPD of CO from Co/Au(111). As with Co/Ag(111), the only peak seen in this temperature range is that of the manipulator. The dotted blue line is a reference measurement of degassing from the manipulator without gas adsorbed on the sample.

The QMS is then positioned directly above the sample with the opening of the pipe very close to the sample surface. This prevents desorbed gas from the sample plate, the manipulator and the filament from being measured by the QMS. Such a setup could be even further improved by adding a separate ion pump behind the QMS.

Another factor contributing to this problem is the temperature gradient across the manipulator. The sample is heated by a resistive heating element, but the temperature is not the same over the entire manipulator. The total measured desorption spectrum therefore includes desorption from many sites at many temperatures.

The sample temperature is measured using a thermocouple attached to the manipulator, not the sample itself. Even though the thermocouple was removed from its original position and moved closer to the sample, there is still a temperature difference between the sample and the value measured. This was attampted handled by using calibration measurements. Since the Eurotherm works by adjusting the heating output as a function of the measured temperature, it will create a linear heating ramp in the spot where the thermocouple is located. This means that the actual heating ramp at the surface is not entirely linear. This problem was not significant for experiments in the $30 - 250°$C range, but for low starting temperatures the heating ramp could not be called linear. In other UHV systems the temperature is measured by placing a thermocouple inside a hole in the crystal.

Since the heating was done using a resistive heating element, the heating rate was limited to around $1\frac{\mathrm{K}}{\mathrm{s}}$. Achieving a higher heating rate would have exceeded the maximum allowed current for the filemant. An alternate method of heating is to place a filament below the sample plate, and heat the sample using an electron stream from the filament to the sample plate (this is also how the e-beam evaporator works).

Last, but not least, it must be mentioned that the choice of CO may also have contributed to this problem. CO is a commonly used gas for this type of experiment because it is well-studied and make a simple component for measurements and comparisons, however it is also one of the most common background gasses in UHV systems. Since a QMS can be set to measure only the pressure of molecules with a single mass, using a different gas would have eliminated much of the degassing signal from the filament, since this is mostly CO.

Chapter 8

Conclusion

Attempt were made at performing TPD experiments from Co/Cu(111) structures, unfortunately they were not successful. Instead the main body of work became the ARPES images recorded at ASTRID in Århus. These images gave information on two features of the samples, the locations of the d-states in the valence band, and the surface states near the Fermi edge.

Studying the EDC curves, containing information on the structure of the valence bands, showed a few things of interest. In the d-band peaks of the Ag 4d state, the individual peaks are places further apart at low coverages than at high. Furthermore, It was seen that the Co d-band peak did not shift noticably when the Co coverage was varied. This indicates that the growth-mode of Co was consistently pseudomorphic during the experiments. Although the Co 3d-band might begin to shift towards their bulk levels with high enough coverages, this was not observed here. Since the goal of these experiments were to study surface states, the coverages were kept fairly low.

The most interesting results from the ARPES experiments were the decreases in the binding energies of the Ag states in the Ag/Cu(111) and Ag/Co/Cu(111) systems. The addition of small amounts of Co under the silver has a clear effect on the binding energies. For higher Co coverages (near 2 ML) the binding energy appears to have risen again a bit, which is explained by an "inverted structures" scheme, in which the Co islands seen at low coverages have been replaced by holes in a Co layer covering almost the entire surface.

The TPD results have been incinclusive, and require re-doing using an improved setup. Suggestions for an improved setup include using a snout to limit the ges entering the mass spectrometer to molecules desorbed from the sample surface. More accurate temperature measurements would also be preferrable.

References

[BWDK09] J. Bork, P. Wahl, L. Diekhöner, and K. Kern. Potential energy landscape of metallic moiré patterns. *New Journal of Physics*, 11, 2009.

[CN03] I. Chorkendorff and J.W. Niemantsverdriet. *Concepts of Modern Catalysis and Kinetics.* Wiley, 2003.

[Dah05] Jens P. Dahl. *Introduction to the Quantum World of Atoms and Molecules.* World Scientific, 2005.

[GNKB09] T.G. Gopakumar, N. Néel, J. Kröger, and R. Berndt. Spatial modulation of d states in a nanoscale co island. *Chemical Physics Letters*, 484:59–63, 2009.

[GPS02] Herbert Goldstein, Charles Poole, and John Safko. *Classical Mechanics.* Addison Wesley, 3. edition, 2002.

[HK84] E. Habenschaden and J. Küppers. Evaluation of flash desorption spectra. *Surface Science*, 138(1):L147 – L150, 1984.

[HN91] Stephen Halloway and Jens Nørskov. Bonding at surfaces, 1991. Lecture notes.

[HN95] B. Hammer and J.K. Nørskov. Why gold is the noblest of all the metals. *Nature*, 376:238–240, 1995.

[Hüf03] Stefan Hüfner. *Photoelectron Spectroscopy.* Springer, 3. edition, 2003.

[Kit05] Charles Kittel. *Introduction to Solid State Physics.* Wiley, 8. edition, 2005.

[LC98] J.H. Larsen and I. Chorkendorff. Enhanced reactivity of pseudomorphic co on cu(111). *Catalysis Letters*, 52:1–5, 1998.

[LK74] Frances M. Lord and J.S. Kittelberger. On the determination of activation energies in thermal desorption experiments. *Surface Science*, 43(1):173 – 182, 1974.

[Lüt01] Hans Lüth. *Solid Surfaces, Interfaces and Thin Films.* Springer, 4. edition, 2001.

[MBR02] Karina Morgenstern, Kai-Felix Braun, and Karl-Heinz Rieder. Surface-state depopulation on small ag(111) terraces. *Physical Review Letters*, 89, 2002.

[MKFR+07] D. Malterre, B. Kierren, Y. Fagot-Revurat, S. Pons, A. Tejeda, C. Didiot, H. Cercellier, and A. Bendounan. Arpes and sts investigation of shockley states in thin metallic films and periodic nanostructures. *New Journal of Physics*, 9, 2007.

[Red62] P.A. Redhead. Thermal desorption of gases. *Vacuum*, 12(4):203 – 211, 1962.

[RG92] José A. Rodriguez and D. Wayne Goodman. The nature of the metal-metal bond in bimetallic surfaces. *Science*, 257(5072):897–903, 1992.

[RHS+97] A. Ruban, B. Hammer, P. Stoltze, H.L. Skriver, and J.K. Nørskov. Surface electronic structure and reactivity of transition and noble metals. *Journal of Molecular Catalysis A: Chemical*, 115(3):421–429, 1997.

[SL10] Gabor A. SomorJai and Yimin Li. *Introduction to Surface Chemistry and Catalysis.* Wiley, 2. edition, 2010.

[WWB+04] M. Wessendorf, C. Wiemann, M. Bauer, M. Aeschlimann, M.A. Schneider, H. Brune, and K. Kern. Electronic surface structure of n-ml ag/cu(111) and cs/n-ml ag/cu(111) as investigated by 2ppe and sts. *Appl. Phys. A*, 78:183–188, 2004.

[YL85] J.J. Yeh and I. Lindau. Atomic subshell photoionization cross sections and asymmetry parameters: $1 \leq z \leq 103$. *Atomic Data and Nuclear Data Tables*, 32(1):1–155, 1985.